acp-2020-643

Song et al. 2020/08/17

We have addressed comments from anonymous referee #1 and made corresponding changes to the manuscript and supplementary material. The revised change-tracked manuscript is attached to this document. Follow-up comments from the anonymous referees and anyone who is interested in this study are highly welcome.

Comments are in black and responses are in blue.

Response to Anonymous Referee #1

Hydroxymethanesulfonate has been recently identified as an important organic sulfate component in atmospheric aerosols in field measurements. Current understanding for this organosulfate chemistry is largely lacking due to sparse field measurement data and modeling studies. This manuscript presents results from a modeling study of aqueous hydroxymethanesulfonate chemistry on a global scale using latest version GEOS-Chem model. Control, default, and ten specific simulations were performed under different modeling settings by incorporating comprehensive SO2 chemistry into GEOS-Chem. The results show both spatial and seasonal variations for the mass concentration and hydroxymethanesulfonate/sulfate ratio distribution and several hotspots were identified including East Asia, Europe, and North America. The paper will improve understanding of atmospheric organosulfate chemistry in aerosol composition, in particular, for regions with high concentrations of hydroxymethanesulfonate such as northern China. The manuscript is well written and it is recommended to be published after a minor revision.

We thank the referee for the positive evaluation and very helpful comments. Our responses to the specific comments are provided below.

Several minor comments include:

1) The differences between control and default simulations were not explicitly shown, specifically, for reaction of SO2 with H2O2, what exactly were the differences between the two simulations since in both cases k4 was taken from Liu et al. (2020) according to Table 1?

As shown in Table 4, there are three major changes in the default simulation compared to the control simulation:
(1) improving treatments of entrainment/detrainment and heterogeneous cloud sulfur chemistry;
(2) adding aerosol water reaction of SO_2 with H_2O_2;
(3) shorter time step for calculating cloud sulfur reactions.

Regarding the 2nd change, the control simulation includes the reaction of SO_2 and H_2O_2 in cloud droplets. This is a classic reaction pathway, and the reaction rates have been well studied and we use the rates from Seinfeld and Pandis (2016). Liu et al. (2020) recently reported the rate constants of SO_2 and H_2O_2 in concentrated aqueous solutions (which are suitable for the application in aerosol water). Thus, for aerosol water, k_4 is multiplied by an enhancement factor EF that is dependent on μ_b (ionic strength) (as shown in Table 1).

We have made this clearer in Sect. 2.5 when introducing the differences between the default and control simulations:

"The third is adding the reaction of H_2O_2 and SO_2 in aerosol water using the kinetic data reported recently by Liu et al. (2020). The control simulation only includes the reaction of H_2O_2 and SO_2 in cloud water."

2) In control simulation, seven pathways were considered for the heterogeneous SO2 reactions. In Fig. 3, only three reactions were shown. The authors should give a clear explanation why those reactions were far more important than others. Several sentences will be beneficial to the readers in order to better understand the order of the importance for the seven reactions.

In Fig.3, we show the probability density distributions of the reaction pathways involving O_3, H_2O_2, and HCHO, as well as the sum of the seven reactions (denoted as "total"). On a global scale, the two key pathways are O_3 and H_2O_2.

The other five pathways, including TMI/O_2, HONO, NO_2, HCHO, and HOBr, are minor pathways. The reason for which we show the data of the pathway involving HCHO is that this paper focuses on the modeling of HMS. In the revised manuscript, we add the data for the other 4 pathways in Fig. 3. It shows that the other 4 pathways are minor compared to those involving O_3 and H_2O_2. We have made corresponding changes in the caption of Fig. 3.

We have also added additional statements in Sect. 2.4 to demonstrate the relative importance of these seven reaction pathways:

"*The rapid consumption of $SO_{2(g)}$ is mainly via O_3 and H_2O_2, as shown in Fig. 3 and Table S1 (statistics of probability distributions). The other five reactions consuming SO_2 (HCHO, TMI+O_2, NO_2, HONO, and HOBr) can be considered as minor pathways."*

We hope that these changes in the revised manuscript can make the comparison of different reaction pathways clearer.

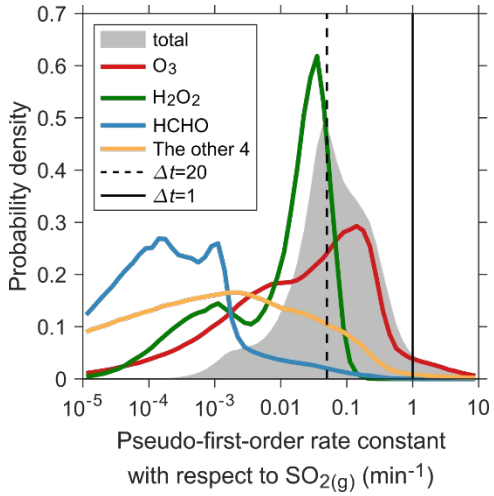

3) Table 5 shows the comparison between simulated and measured values for the HMS to sulfate or MSA. Since the techniques used for measurements of HMS were significantly different which would affect the accuracy. It would be beneficial to point this out in Sect. 3.4.

We have added one sentence in Sect. 3.4 when describing the measurements of HMS:

"The measurement techniques of HMS in different studies have been different (Table 5) and their effects on the reported results are unclear."

We have also updated Table 5 in order to present the exact methods of HMS measurements in different studies. Please find them in the notes of Table 5.

Table 5. Comparison between observations and model simulations.

Location	Year and season	Observed molar ratio	Default	Control	Reference and note
New Mexico, USA	1997 Summer	HMS/SO_4^{2-} < 0.2%	0.3%	2%	Dixon and Aasen (1999); note *a*
Germany	2009/10 All Year	HMS/SO_4^{2-} = 2%	5%	16%	Scheinhardt et al. (2014); note *b*
Beijing, China	2015/16 and 2016/17 Winter	HMS/SO_4^{2-} = 11%	13%	10%	Ma et al. (2020); note *c*
Osaka Bay, Japan	1998/99 Spring, Summer	HMS/MSA = 1	3	20	Suzuki et al. (2001); note *d*

[a]PM_1 (particles smaller than 1 μm) samples of 11 were collected with each sampled for several days. HMS detection method: ion chromatography.
[b]Size-segregated (5 stages under 10 μm) daily aerosol samples of 154 data sets were collected at 9 sites. HMS detection method: capillary electrophoresis.
[c]$PM_{2.5}$ samples of 77 were collected with 69 daily and 8 half-day samples. HMS detection method: ion chromatography.
[d]Size-segregated (4 stages under 7 μm) aerosol samples of 4 data sets were collected with each sampled for 11–25 days. HMS detection method: proton nuclear magnetic resonance (^{1}H NMR).

4) The sensitivity simulation was conducted using 10 min as delta t (L26 on p11). Why 10 min rather than for example 5 min was used? Using a delta t of 5 min may correspond to median probability density in a residence time range of 1 to 20 min as shown in Fig. 3.

As described in Section 2.2, in the standard model, the time step (also known as the transport operator duration) for species advection, vertical mixing, and convection is set to 10 min. The time step (also known as the chemistry operator duration) is 20 min for emissions, dry deposition, photolysis, and chemistry, as recommended by Philip et al. (2016). The chemistry operator duration must be an integer multiple of the transport operator duration. Consequently, we can only use 10 min in this sensitivity test.

Philip, S., Martin, R. V., and Keller, C. A.: Sensitivity of chemistry-transport model simulations to the duration of chemical and transport operators: a case study with GEOS-Chem v10-01, Geosci. Model Dev., 9, 1683-1695, 10.5194/gmd-9-1683-2016, 2016.

5) Several typos or corrections:

L17 on p6, not quite understand what does this mean?" under the dark conditions of sample storage and treatment";

This statement is from the review article by Tilgner and Herrmann (2018). In the bulk measurements, aerosol samples are usually collected on a filter and subsequently diluted for analysis, while cloud water is sampled in the bulk. Both samples are subject to storage for a certain time duration before analysis. The sample storage and treatment are usually in dark conditions because the we do not want to trigger new photochemical reactions during these processes. The sample storage and treatment under the dark conditions may lead to an underestimation in aqueous OH concentrations. This is because in the real atmosphere, there are replenishments of OH and other oxidants from the gas phase, whereas in the dark environment, such replenishments do not exist.

In the revised manuscript, we cite this reference by Tilgner and Herrmann at the end of this sentence. This thorough review article has also been cited several times elsewhere in this manuscript.

Tilgner, A., and Herrmann, H.: Tropospheric Aqueous-Phase OH Oxidation Chemistry: Current Understanding, Uptake of Highly Oxidized Organics and Its Effects, in: Multiphase Environmental Chemistry in the Atmosphere, ACS Symposium Series, 1299, American Chemical Society, 49-85, 2018.

L1 on p10, it is suggested to rewrite "the reactants' Henry's law constants" to "the Henry's law constants of the reactants";

Corrected according to this comment.

L12 on p14, for the next? Is something missed after "next".

Corrected. Added "time step" after "next".

Global modeling of heterogeneous hydroxymethanesulfonate chemistry

Shaojie Song[1], Tao Ma[2], Yuzhong Zhang[3,4], Lu Shen[1], Pengfei Liu[5], Ke Li[1], Shixian Zhai[1], Haotian Zheng[1,2], Meng Gao[6], Fengkui Duan[2], Kebin He[2], Michael B. McElroy[1]

[1]School of Engineering and Applied Sciences, Harvard University, Cambridge, MA 02138, USA
[2]State Key Joint Laboratory of Environment Simulation and Pollution Control, School of Environment, State Environmental Protection Key Laboratory of Sources and Control of Air Pollution Complex, Beijing Key Laboratory of Indoor Air Quality Evaluation and Control, Tsinghua University, Beijing 100084, China
[3]School of Engineering, Westlake University, Hangzhou 310024, Zhejiang, China
[4]Institute of Advanced Technology, Westlake Institute for Advanced Study, Hangzhou 310024, Zhejiang, China
[5]School of Earth and Atmospheric Sciences, Georgia Institute of Technology, Atlanta, GA 30332, USA
[6]Department of Geography, State Key Laboratory of Environmental and Biological Analysis, Hong Kong Baptist University, Hong Kong SAR, China

Correspondence: Shaojie Song (songs@seas.harvard.edu)

Abstract. Hydroxymethanesulfonate (HMS) has recently been identified as an abundant organosulfur compound in aerosols during winter haze episodes in northern China. It has also been detected in other regions, although the concentrations are low. Because of the sparse field measurements, the global significance of HMS and its spatial and seasonal patterns remain unclear. Here, we implement HMS chemistry into the GEOS-Chem chemical transport model and conduct multiple global simulations. The developed model accounts for cloud entrainment and gas–aqueous mass transfer within the rate expressions for heterogeneous sulfur chemistry. Our simulations can generally reproduce the available HMS observations, and show that East Asia has the highest HMS concentration, followed by Europe and North America. The simulated HMS shows a seasonal pattern with higher values in the colder period. Photochemical oxidizing capacity affects the competition of formaldehyde with oxidants (such as ozone and hydrogen peroxide) for sulfur dioxide and is a key factor influencing the seasonality of HMS. The highest average HMS concentration (1–3 μg m^{-3}) and HMS/sulfate molar ratio (0.1–0.2) are found in northern China winter. The simulations suggest that aqueous clouds act as the major medium for HMS chemistry while aerosol liquid water may play a role if its rate constant for HMS formation is greatly enhanced compared to cloud water.

1 Introduction

Organosulfur compounds (OSs) have been detected in secondary organic aerosols (SOA). The OSs affect the physicochemical properties of aerosols such as hygroscopicity, acidity, and viscosity, and ultimately the climate and health effects of aerosols (Surratt et al., 2007; Farmer et al., 2010; Sorooshian et al., 2015; Estillore et al., 2016; Riva et al., 2019). The identified OSs include organosulfates ($ROSO_3^-$), sulfoxides (RSOR'), sulfones (RSO_2R'), and sulfonates (RSO_3^-) (Brüggemann et al., 2020). Sulfonates include methanesulfonate ($CH_3SO_3^-$, deprotonated MSA, methanesulfonic acid) and hydroxyalkylsulfonates ($RCH(OH)SO_3^-$) (Song et al., 2019a). These classes of OSs may differ widely in their formation mechanisms, concentration

levels, and spatiotemporal distributions. Organosulfates and MSA are the two most studied OSs species or classes (Bates et al., 1992; Huang et al., 2017; Brüggemann et al., 2020). Organosulfates are primarily formed by the reactive uptake of gas-phase epoxides on acidic sulfate particles (Froyd et al., 2010; Surratt et al., 2010; Xu et al., 2015). The most abundant organosulfate observed in ambient fine particulate matter ($PM_{2.5}$) is the isoprene-derived methyltetrol sulfate ($C_5H_{11}SO_7^-$), with an average concentration of 1.8 μg m^{-3} found during August 2015 in Atlanta, Georgia, USA (Hettiyadura et al., 2019). MSA is produced primarily by the oxidation of biogenic dimethyl sulfide (DMS) and is likely the major organosulfur species in many regions over the oceans (Chen et al., 2018; Hodshire et al., 2019). The concentrations of aerosol-phase MSA in marine environments are on the order of tens to a few hundreds of ng m^{-3} (Phinney et al., 2006; Sciare et al., 2009; Huang et al., 2017).

Very recently, high mass concentrations of hydroxymethanesulfonate (HMS, $CH_2(OH)SO_3^-$), a hydroxyalkylsulfonate species, have been detected in winter Beijing, China using an aerosol mass spectrometer by Song et al. (2019a) and using an improved ion chromatography method by Ma et al. (2020). The mass spectrometry quantification of HMS in ambient aerosols may be subject to the interference of other inorganic and organic sulfur compounds, as suggested by Dovrou et al. (2019). The average HMS concentration in 2015/16 and 2016/17 winters in Beijing was observed to be 1.9 μg m^{-3} (Ma et al., 2020). The highest daily average HMS concentration reached 15 μg m^{-3}, accounting for 6% of $PM_{2.5}$ concentration (Ma et al., 2020). Song et al. (2019a) argued that HMS was likely the major organosulfur compound during winter haze events in northern China. Prior to the two studies, only low levels of HMS, with averages on the order of 0.01 μg m^{-3}, had been observed in the United States, Japan, and Germany (Dixon and Aasen, 1999; Suzuki et al., 2001; Scheinhardt et al., 2014). Generally, existing observational studies indicate significant spatial variations in HMS.

Our knowledge of the chemical mechanism for HMS stems largely from studies in the 1980s when it was recognized as part of the aqueous sulfur chemistry (Pandis and Seinfeld, 1989). Field measurements of cloud water in the Los Angeles Basin showed the coexistence of H_2O_2 and S(IV) that was much larger than expected based on the phase equilibrium with gaseous SO_2 (Richards et al., 1983). The formation of HMS by the reaction of dissolved SO_2 and HCHO was postulated, and then proved, to explain the observed excess of S(IV) (Munger et al., 1986). The laboratory experiments from several groups determined the kinetics and thermodynamics of HMS reactions in aqueous solutions (Boyce and Hoffmann, 1984; Deister et al., 1986; Dong and Dasgupta, 1986; Kok et al., 1986; Olson and Fessenden, 1992). Briefly, both formation and decomposition of HMS depend strongly on pH, i.e., the hydrogen ion activity expressed on a logarithmic scale. HMS is resistant to oxidation by H_2O_2 and O_3 but reacts with hydroxyl radicals (OH) in the aqueous phase. These studies suggested that the atmospheric conditions favorable for the formation and stability of HMS involved abundant gas-phase SO_2 and HCHO, high aqueous water content, low temperature, intermediate pH, and low photochemical activity.

The integration and reconciliation of data from field observations, laboratory experiments, and chemical modeling are crucial for obtaining a better understanding of how HMS is processed in the atmosphere. This study offers a global chemical simulation

of HMS using the GEOS-Chem chemical transport model to explore its large-scale spatiotemporal distribution. Multiple model simulations are designed and conducted. The model is driven by the kinetic and thermodynamic data obtained from available laboratory experiments. The simulated results are compared with field observations. The HMS chemistry is heterogeneous in nature since the reactions occur in the aqueous phase with reactants transported from the gas phase (Jacob, 2000). Sometimes heterogeneous chemistry is referred to as multiphase chemistry (Ravishankara, 1997). Both aqueous cloud droplets (Jacob, 1986; Olson and Hoffmann, 1989; Moch et al., 2018) and aqueous aerosols (Song et al., 2019a; Ma et al., 2020) have been suggested to provide the media for HMS reactions. However, kinetic and thermodynamic data have been determined only in dilute solutions, which are suitable for application in clouds. The lack of corresponding data in concentrated solutions poses a key challenge to modeling HMS chemistry for aerosol water. Therefore, we assume that cloud water serves as the only medium in the control and default simulations. The role of aerosol water is explored through several sensitivity simulations. As shown in Figure 1, the overall heterogeneous reaction rates are controlled not only by rate constants in the aqueous phase but also by mass transfer limitations between the gas and aqueous phases (Jacob, 1986; Ravishankara, 1997; Seinfeld and Pandis, 2016). In partly cloudy conditions, heterogeneous reactions may also be influenced by the entrainment and detrainment of air into and out from clouds (Fig. 1) (Holmes et al., 2019). Compared with the control simulation that follows the parameterization in the standard GEOS-Chem model, the default simulation improves treatments of entrainment and mass transfer processes for heterogeneous cloud sulfur chemistry. Aerosol water chemistry in the sensitivity simulations also considers the physiochemical processes in Fig. 1, allowing an evaluation of the importance of the two aqueous media.

This article is organized as follows. In the Method section, we first provide an overview of the aqueous chemical reactions for HMS, including its formation, decomposition, and oxidation (Sect. 2.1). From existing laboratory studies, we critically estimate the best values and uncertainties of their rate constants. The general configuration of the GEOS-Chem model is described in Sect. 2.2, including its version, simulation period, spatial and temporal resolutions, meteorological field, chemical mechanisms, and underlying emissions. A brief introduction of sulfur simulation in the standard model is given in Sect. 2.3. The two major simulations in this study, control and default, are described in Sect. 2.4 and 2.5, respectively. Based on settings in the standard model, the control simulation implements heterogeneous HMS chemistry using cloud as the only aqueous medium. We find that the in-cloud SO_2 titration by various reactants is inappropriately represented in the control simulation, very likely leading to an overestimation of HMS formation. The default simulation fixes this issue. Sect. 2.6 describes the sensitivity simulations designed to investigate the key factors leading to uncertainty in the modeled HMS levels. In the Results and discussion section, we first show in Sect. 3.1 the spatial and seasonal distributions of HMS from the default simulation and discuss the underlying factors. Differences in the modeled HMS between the default and control simulations are presented and discussed in Sect. 3.2. Sect. 3.3 demonstrates the key uncertain parameters and processes in the HMS model identified from sensitivity simulations. Sect. 3.4 compares the observations of HMS in different regions with model results. The knowledge gained in this study and the remaining gaps are summarized in Sect. 3.5. Finally, the conclusions are given in Sect. 4.

2 Methods

2.1 Kinetics and thermodynamics of HMS chemistry

Hydroxymethanesulfonic acid (HMSA, $CH_2(OH)SO_3H$) is a diacid with $pK_{a1} < 0$ (R1) and $pK_{a2} \sim 12$ (R2). Thus, it primarily exists as HMS ($CH_2(OH)SO_3^-$) in tropospheric clouds and aerosols. In the aqueous phase, HMS is produced by the nucleophilic addition of HSO_3^- and SO_3^{2-} to the carbonyl C atom of HCHO (R3–R6). As SO_3^{2-} is a much stronger nucleophile than HSO_3^-, the rate constant of $HCHO_{(aq)} + SO_3^{2-}$, k_2, is a few orders of magnitude higher than that of $HCHO_{(aq)} + HSO_3^-$, k_1, as shown in Table 1. $HCHO_{(aq)}$ refers to the free, unhydrated formaldehyde dissolved in the aqueous phase, and maintains an equilibrium with its hydrated form, $CH_2(OH)_2$ (methylene glycol). The equilibrium constant of (R7), K_h, represents the extent of hydration (Eq. 1). (R1–R6) are all reversible and can be summarized by (R8). $SO_{2(aq)}^T$ is the sum of $SO_2{\cdot}H_2O$, HSO_3^-, and SO_3^{2-} (Eq. 2). k_f ($M^{-1}s^{-1}$) and k_d (s^{-1}) represent the forward and backward reaction (HMS formation and decomposition) rate constants of (R8) and K_{eq} (M^{-1}) is its equilibrium constant (Eq. 3). k_f is a combination of k_1 and k_2 weighted by the fractions of HSO_3^- and SO_3^{2-} in $SO_{2(aq)}^T$ (Eqs. 4–6). K_{s1} and K_{s2} denote the first and second dissociation constants for dissolved SO_2 (Table 2). Figure 2 shows the values of k_f and k_d obtained from the available laboratory experiments as a function of pH (Blackadder and Hinshelwood, 1958; Sørensen and Andersen, 1970; Boyce and Hoffmann, 1984; Deister et al., 1986; Dong and Dasgupta, 1986; Kok et al., 1986; Lagrange et al., 1999). In general, we find a large discrepancy for k_f and good agreement for k_d.

$$CH_2(OH)SO_3H \leftrightarrow CH_2(OH)SO_3^- + H^+ \quad \text{(R1)}$$

$$CH_2(OH)SO_3^- \leftrightarrow CH_2(O^-)SO_3^- + H^+ \quad \text{(R2)}$$

$$SO_2{\cdot}H_2O \leftrightarrow HSO_3^- + H^+ \quad \text{(R3)}$$

$$HSO_3^- \leftrightarrow SO_3^{2-} + H^+ \quad \text{(R4)}$$

$$HCHO_{(aq)} + HSO_3^- \overset{k_1}{\leftrightarrow} CH_2(OH)SO_3^- \quad \text{(R5)}$$

$$HCHO_{(aq)} + SO_3^{2-} \overset{k_2}{\leftrightarrow} CH_2(O^-)SO_3^- \quad \text{(R6)}$$

$$HCHO_{(aq)} + H_2O \leftrightarrow CH_2(OH)_2 \quad \text{(R7)}$$

$$HCHO_{(aq)} + SO_{2(aq)}^T \leftrightarrow HMS \quad \text{(R8)}$$

$$K_h = [CH_2(OH)_2]/[HCHO]_{aq} \quad (1)$$

$$\left[SO_2^T\right]_{aq} = [SO_2{\cdot}H_2O] + [HSO_3^-] + \left[SO_3^{2-}\right] \quad (2)$$

$$K_{eq} = [HMS]/\left([HCHO]_{aq}\left[SO_2^T\right]_{aq}\right) = k_f/k_d \quad (3)$$

$$k_f = k_{10}x_{HSO_3^-} + k_{11}x_{SO_3^{2-}} \quad (4)$$

$$x_{HSO_3^-} = [HSO_3^-]/\left[SO_2^T\right]_{aq} = K_{s1}[H^+]/([H^+]^2 + K_{s1}[H^+] + K_{s1}K_{s2}) \quad (5)$$

$$x_{SO_3^{2-}} = \left[SO_3^{2-}\right]/\left[SO_2^T\right]_{aq} = K_{s1}K_{s2}/([H^+]^2 + K_{s1}[H^+] + K_{s1}K_{s2}) \quad (6)$$

2.1.1 HMS formation

Boyce and Hoffmann (1984) determined the following kinetic parameters at ionic strength μ = 1 M, pH from 0 to 3.5: $k_1 = 7.9 \times 10^2$ M^{-1} s^{-1} and $k_2 = 2.5 \times 10^7$ M^{-1} s^{-1} (both at 298 K). The enthalpies of activation $\Delta^{\ddagger}H_1$ and $\Delta^{\ddagger}H_2$ were 25 kJ mol^{-1} and 20 kJ mol^{-1}, respectively. These parameters were calculated assuming $K_{s1} = 1.45 \times 10^{-2}$ M and $K_{s2} = 6.31 \times 10^{-8}$ M, which were in fact for dilute solutions ($\mu \approx 0$ M). According to Boyce and Hoffmann (1984), application of the Davies equation to correct for the ionic strength effects on K_{s1} and K_{s2} yielded $k_1 = 4.5 \times 10^2$ $M^{-1}s^{-1}$, $k_2 = 5.4 \times 10^6$ $M^{-1}s^{-1}$ (both at 298 K), $\Delta^{\ddagger}H_1 = 22$ kJ mol^{-1}, and $\Delta^{\ddagger}H_2 = 21$ kJ mol^{-1}. Boyce and Hoffmann (1984) also used a higher K_h of 1.8×10^3 than the value of 1.3×10^3 obtained in a more recent study by Winkelman et al. (2002) (Table 2). We further adjust the kinetics based on this recent K_h and obtain $k_1 = 3.2 \times 10^2$ $M^{-1}s^{-1}$ and $k_2 = 3.8 \times 10^6$ $M^{-1}s^{-1}$.

Therefore, two sets of HMS formation kinetic data can be obtained from Boyce and Hoffmann (1984) and are designated here as the high and low rate constants, as shown in Table 1 and Fig. 2. The calculated high and low k_f differ by a factor of about 3 at pH < 2 and by a factor of about 6 at pH > 4. The low k_f agrees very well (within a factor of 1.1) with the results determined by Kok et al. (1986) and Deister et al. (1986) at higher pH 4, 5, and 5.6 (Fig. 2). The low kinetic data are also closer to the rate constants from the recent quantum chemical calculations by Zhang et al. (2019) ($k_1 = 0.9$ $M^{-1}s^{-1}$, $k_2 = 2 \times 10^6$ $M^{-1}s^{-1}$, at 298 K). Consequently, the low formation rate constants from Boyce and Hoffmann (1984) are adopted for the default model simulation, while the high ones are used in a sensitivity simulation. Lagrange et al. (1999) proposed another value of k_f which was about 1–4 orders of magnitude smaller than the low k_f from Boyce and Hoffmann (1984) at pH > 4 (Fig. 2). The simulated HMS concentration is negligible everywhere when applying the k_f from Lagrange et al. (1999) in the model, and thus, will not be discussed further.

2.1.2 HMS decomposition

The most complete analysis of K_{eq} was done by Deister et al. (1986). We calculate the expression of k_d using the low k_f from Boyce and Hoffmann (1984) and K_{eq} from Deister et al. (1986) (Eq. 3 and Table 1). As shown in Fig. 2, k_d estimated in this way agrees within a factor of about 2 with results from the other laboratory studies (Blackadder and Hinshelwood, 1958; Sørensen and Andersen, 1970; Dong and Dasgupta, 1986; Kok et al., 1986; Lagrange et al., 1999). Therefore, this expression of k_d is adopted in the default simulation, and its value is doubled in a sensitivity simulation. If we use the high k_f from Boyce and Hoffmann (1984) and the K_{eq} from Deister et al. (1986), we will obtain a k_d that is several times higher than estimates from the other studies. This may serve as circumstantial evidence in favor of the low k_f.

2.1.3 HMS oxidation

HMS is resistant to oxidation by H_2O_2 and O_3 but can be oxidized by OH in the aqueous phase (Martin et al., 1989; Olson and Fessenden, 1992). (R9) produces HCHO and peroxysulfate radical (SO_5^-) with a rate constant of 2.7×10^8 M^{-1} s^{-1} (Olson and

Fessenden, 1992) (Table 1). This value is lower by a factor of about 4 than the results reported in two earlier laboratory studies (Martin et al., 1989; Deister et al., 1990). Olson and Fessenden (1992) argued that these two studies were subject to artifacts and interferences from secondary reactions.

$$\mathrm{HMS} + \mathrm{OH_{(aq)}} \xrightarrow{\mathrm{O_2}} \mathrm{HCHO_{(aq)}} + \mathrm{SO_5^-} + \mathrm{H_2O} \qquad \text{(R9)}$$

The second source of uncertainty in (R9) arises from estimating aqueous OH concentrations. Aqueous OH is a short-lived species that can be transferred from the gas phase and generated/scavenged in the aqueous phase. Its sources and sinks, which are linked to photochemical processes (e.g., photolysis of nitrate and peroxides), transition metal ions (Fenton reactions), and/or reactions with halogen anions and organic matters, are not yet fully understood (Tilgner and Herrmann, 2018). Currently, there exist significant discrepancies between the modeled and measured $[OH]_{aq}$ levels. A comprehensive overview has shown that $[OH]_{aq}$ from different model studies ranges from 3×10^{-15} M to 8×10^{-12} M for cloud droplets and from 1×10^{-16} M to 8×10^{-12} M for aqueous aerosols, and that, on the other hand, data ranges of the measured $[OH]_{aq}$ are $0.5–7 \times 10^{-15}$ M for clouds and $0.1–6 \times 10^{-15}$ M for aerosols (Tilgner and Herrmann, 2018). On average, the modeled $[OH]_{aq}$ is two orders of magnitude higher than the measured values. This large gap is believed to result from the limitations of both models and measurements. The bulk measurements of $[OH]_{aq}$ may underestimate its concentrations in real aerosols and clouds due to lack of replenishment of important oxidations and OH precursors from the gas phase under the dark conditions of sample storage and treatment (Tilgner and Herrmann, 2018). On the other hand, the multiphase models may significantly overpredict $[OH]_{aq}$ because they only partially consider the complex organic aqueous chemistry. The reasonable estimates of $[OH]_{aq}$ in real aerosols and clouds seem to be one order of magnitude lower than modeled concentrations and one order of magnitude higher than measured levels (Tilgner and Herrmann, 2018). Since GEOS-Chem does not have a detailed representation of aqueous OH chemistry, we simply estimate $[OH]_{aq}$ using the modeled $[OH]_g$ and a pseudo Henry's law constant H^*_{OH} (Eq. 7). In the default simulation, H^*_{OH} is set to 4×10^{-20} M cm^3 molecules^{-1}. H^*_{OH} is more than one order of magnitude lower than its intrinsic Henry's law constant, H_{OH} (Table 2), reflecting our presumption that the various organic and inorganic compounds in the aqueous phase act as a net sink for OH radicals. A global mean $[OH]_g$ of about 1×10^6 molecules cm^{-3} implies a mean $[OH]_{aq}$ of 4×10^{-14} M, one order of magnitude higher than the mean of the above-mentioned measured $[OH]_{aq}$.

$$[\mathrm{OH}]_{aq} = [\mathrm{OH}]_g \times H^*_{OH} \qquad (7)$$

The products of (R9) are $HCHO_{(aq)}$ and SO_5^-. Interestingly, the net effect of HMS formation (R8) and its subsequent oxidation (R9) is the oxidation of $SO^T_{2(aq)}$ by $OH_{(aq)}$, which represents thus an indirect oxidation pathway for SO_2. The sinks for SO_5^- are mainly the reactions with O_2^-, $HCOO^-$, and itself (R10–R12). The reaction of SO_5^- and HSO_3^- is slow (Jacob et al., 1989). The peroxymonosulfate radical (HSO_5^-) produced by (R10–R11) can oxidize HSO_3^- to sulfate (R13) with a similar rate constant to $H_2O_2 + HSO_3^-$ (Betterton and Hoffmann, 1988). The sulfate radical (SO_4^-) produced by (R12) is a very strong oxidant and can

react rapidly with HSO_3^- and SO_3^{2-} (R14–R15) as well as with many other species such as Cl^-, NO_2^-, O_2^-, $HCOO^-$, and HO_2 (Jacob, 1986). The rate constants for (R10–R15) can be found in Jacob et al. (1989). It is convenient to define the sulfate yield as the number of SO_4^{2-} ions produced due to each attack of $OH_{(aq)}$ on HMS. If SO_5^- reacts with O_2^-/$HCOO^-$ (R10–R11) and the product HSO_5^- oxidizes HSO_3^- (R13), the yield is 2. If SO_5^- undergoes self-reaction (R12) and the produced SO_4^- reacts with HSO_3^-/ SO_3^{2-} (R14–R15), a reaction chain is triggered as the products include SO_5^-. In certain conditions, the sulfate yield can reach several tens or more (Jacob et al., 1989). However, as mentioned above, other oxidizable species also compete for SO_4^-, thereby terminating this chain and leading to a sulfate yield of 1. In remote environments where SO_2 is very low, HSO_5^- may be a stable species, resulting in a sulfate yield < 1. Our low $[OH]_{aq}$ assumption implies the existence of important oxidizable species, and therefore, the chain propagation is limited. In our simulations, the sulfate yield is assumed to be 2.

$$SO_5^- + O_2^- \xrightarrow{H_2O} HSO_5^- + O_2 + OH^- \quad \text{(R10)}$$

$$SO_5^- + HCOO^- \xrightarrow{O_2} HSO_5^- + O_2^- + CO_2 \quad \text{(R11)}$$

$$SO_5^- + SO_5^- \rightarrow 2SO_4^- + O_2 \quad \text{(R12)}$$

$$HSO_5^- + HSO_3^- \rightarrow 2SO_4^{2-} + 2H^+ \quad \text{(R13)}$$

$$SO_4^- + HSO_3^- \xrightarrow{O_2} SO_4^{2-} + SO_5^- + H^+ \quad \text{(R14)}$$

$$SO_4^- + SO_3^{2-} \xrightarrow{O_2} SO_4^{2-} + SO_5^- \quad \text{(R15)}$$

2.1.4 Phase equilibrium

The gas/aqueous phase equilibriums of HCHO (R16) and SO_2 (R17) are described by intrinsic Henry's law constants, H_{HCHO} and H_{SO_2}, respectively (Table 2). $HCHO_{(aq)}$ is subject to hydration, and the apparent Henry's law constant, H^*_{HCHO}, is much larger than H_{HCHO} (Eq. 8). $SO_2{\cdot}H_2O$ dissociates twice in the aqueous phase and thus $H^*_{SO_2}$ depends on pH (Eq. 9). The rates for the hydration of $HCHO_{(aq)}$ (k_h in Table 2) and the acid dissociations of $SO_2{\cdot}H_2O$ (Schwartz and Freiberg, 1981) are fast enough and we assume that these reactions are always in equilibrium.

$$HCHO_{(g)} \leftrightarrow HCHO_{(aq)} \quad \text{(R16)}$$

$$SO_{2(g)} + H_2O \leftrightarrow SO_2{\cdot}H_2O \quad \text{(R17)}$$

$$H^*_{HCHO} = \left([CH_2(OH)_2] + [HCHO]_{aq}\right)/[HCHO]_g = H_{HCHO}(1 + K_h) \cong H_{HCHO}K_h \quad (8)$$

$$H^*_{SO_2} = \left[SO_2^T\right]_{aq}/[SO_2]_g = H_{SO2}(1 + K_{s1}/[H^+] + K_{s1}K_{s2}/[H^+]^2) \quad (9)$$

2.2 General model description

We perform global simulations of heterogeneous HMS chemistry using the three-dimensional GEOS-Chem chemical transport model (version 12.1.0, Doi: 10.5281/zenodo.1553349, last access: 10 June 2020). The simulations are driven by the MERRA-2 (Modern-Era Retrospective analysis for Research and Applications, version 2) reanalysis meteorology from the NASA Goddard Earth Observing System (Gelaro et al., 2017). The original MERRA-2 has a resolution of 0.625° (longitude) × 0.5°

(latitude) and is degraded to 5° × 4° for input into the simulations. There are 47 vertical layers in the atmosphere from surface to the mesosphere. The simulations are conducted for 18 months starting from March 2015. The first 6 months are used for initialization and we focus on the 1-year simulation results from September 2015 to August 2016. These months are selected to obtain a continuous boreal winter. We use the tropospheric chemistry mechanism with detailed reactions for O_3-NO_x-VOC (volatile organic compound)-aerosol-halogen interactions. The time step for species advection, vertical mixing, and convection is set to 10 min. The time step is 20 min for emissions, dry deposition, photolysis, and chemistry, as recommended by Philip et al. (2016). The simulated aerosol species include secondary inorganic (sulfate, nitrate, and ammonium) and organic aerosols, primary organic aerosols, black carbon, dust, and sea salt.

Emissions are calculated using HEMCO (the Harvard-NASA Emissions Component, version v2.1.010) (Keller et al., 2014). The global anthropogenic emissions of SO_2, NO_x, NH_3, CO, VOCs, black carbon, and organic carbon are from the Community Emissions Data System (CEDS) (Hoesly et al., 2018). Emissions are overwritten by regional inventories wherever available: EMEP (European Monitoring and Evaluation Programme) over Europe (www.emep.int/index.html, last access: 10 June 2020), MIX over Asia (Li et al., 2017), DICE (Diffuse and Inefficient Combustion Emissions) over Africa (Marais and Wiedinmyer, 2016), NEI (National Emissions Inventory) over the United States (Travis et al., 2016), CAC (Criteria Air Contaminants) over Canada (wiki.seas.harvard.edu/geos-chem/index.php/CAC_anthropogenic_emissions, last access: 10 June 2020), and MEIC (Multi-resolution Emission Inventory) over China (Zheng et al., 2018). Primary emissions of sulfate constitute 1.4%–5% of total anthropogenic sulfur emissions in different regions of the world. Aircraft emissions are from the Aviation Emissions Inventory Code (Simone et al., 2013). Biomass burning emissions are from the Global Fire Emissions Database (GFED, version 4) (van der Werf et al., 2017). Biogenic VOC emissions are calculated by the Model of Emissions of Gases and Aerosols from Nature (MEGAN, version 2.1) (Guenther et al., 2012). Mineral dust emissions follow Duncan et al. (2007) and are distributed in one fine and three coarse size bins. Anthropogenic emissions of fine dust aerosols are from the Anthropogenic Fugitive, Combustion, and Industrial Dust (AFCID) inventory (Philip et al., 2017). Sea salt aerosols in two size bins (fine and coarse) are simulated based on Jaeglé et al. (2011). Other emissions include volcanic SO_2 emissions (Ge et al., 2016), oceanic DMS emissions (Lana et al., 2011), lightning and soil NO_x emissions (Hudman et al., 2012; Murray et al., 2012), and natural NH_3 emissions from the GEIA (Global Emissions InitiAtive) inventory (www.geiacenter.org, last access: 10 June 2020).

Because of the importance of acidity for heterogeneous HMS chemistry, more details are provided for the calculation of cloud water and aerosol pH. The standard model calculates cloud water pH iteratively with an initial estimate of 4.5, as described in Alexander et al. (2012). The ions considered in the electroneutrality equation are NH_4^+, H^+, OH^-, SO_4^{2-}, NO_3^-, HSO_3^-, SO_3^{2-}, HCO_3^-, and CO_3^{2-}. HSO_3^-/SO_3^{2-} and HCO_3^-/CO_3^{2-} are from the scavenging of SO_2 and CO_2. SO_4^{2-} is assumed to be the only form of sulfate and is obtained from the cloud scavenging of aerosols. NH_4^+ and NO_3^- are from the scavenging of both aerosols and gases (NH_3 and HNO_3). The scavenging efficiencies of aerosols and gases are assumed to be 0.7 and unity, respectively. The ISORROPIA II (version 2.2) thermodynamic equilibrium model (Fountoukis and Nenes, 2007) is used to calculate the

inorganic aerosol water content (m^3 H_2O m^{-3} air) and pH, including the following gas and aerosol species: NH_3, HNO_3, ammonium, nitrate, sulfate, and fine sea-salt aerosols.

2.3 Sulfur simulation in the standard model

The sulfur simulation in GEOS-Chem has been developed and improved based on multiple studies (Chin et al., 2000; Park et al., 2004; Alexander et al., 2005, 2009; Chen et al., 2017; Shao et al., 2019). The simulated sulfur species include DMS, SO_2, MSA, and sulfate. It includes primary emissions of DMS, SO_2, and sulfate (Sect. 2.2). SO_2, MSA, and sulfate can be formed also by chemical reactions. The model contains three gas-phase reactions of DMS oxidation, producing SO_2 and MSA (R18–R20). An expanded chemistry mechanism for DMS can be found in Chen et al. (2018). The oxidation of SO_2 to sulfate occurs in the gas phase by OH (R21) and in the aqueous clouds. The aqueous-phase oxidants are O_3, H_2O_2, O_2 (catalyzed by transition metal ions Mn^{2+} and Fe^{3+}), and HOBr (R22–R25). The effect of the heterogeneity in cloud droplet pH on sulfate production rates is accounted for using the parameterization by Yuen et al. (1996) and Fahey and Pandis (2001). This parameterization is restricted over the ocean since the heterogeneity in pH is believed to be caused by alkaline sea-salt aerosols (Alexander et al., 2012). The model also includes the oxidation of SO_2 by O_3 on sea-salt aerosol surface (R26) (Alexander et al., 2005).

$$DMS_{(g)} + OH_{(g)} \rightarrow SO_{2(g)} + CH_3O_{2(g)} + HCHO_{(g)} \quad \text{(R18)}$$

$$DMS_{(g)} + OH_{(g)} \rightarrow 0.75SO_{2(g)} + 0.25MSA_{(g)} \quad \text{(R19)}$$

$$DMS_{(g)} + NO_{3(g)} \rightarrow SO_{2(g)} + CH_3O_{2(g)} + HCHO_{(g)} + HNO_{3(g)} \quad \text{(R20)}$$

$$SO_{2(g)} + OH_{(g)} \xrightarrow{M} H_2SO_{4(g)} + HO_{2(g)} \quad \text{(R21)}$$

$$SO_{2(aq)}^{T} + O_{3(aq)} \rightarrow SO_4^{2-} + O_{2(aq)} \quad \text{(R22)}$$

$$SO_{2(aq)}^{T} + H_2O_{2(aq)} \rightarrow SO_4^{2-} + H_2O \quad \text{(R23)}$$

$$SO_{2(aq)}^{T} + O_{2(aq)} \xrightarrow{Mn^{2+},Fe^{3+}} SO_4^{2-} \quad \text{(R24)}$$

$$SO_{2(aq)}^{T} + HOBr_{(aq)} \rightarrow SO_4^{2-} + HBr_{(aq)} \quad \text{(R25)}$$

$$SO_{2(g)} + O_{3(g)} + \text{fine sea salt} \rightarrow SO_4^{2-} + O_2 \quad \text{(R26)}$$

2.4 Control simulation

Based on the standard model v12.1.0, we implement heterogeneous HMS chemistry and assume that cloud water provides the only aqueous medium. As described in Sect. 2.1, HMS is produced by dissolved SO_2 and HCHO, undergoes decomposition, and is oxidized to sulfate by aqueous OH. Two other cloud sulfate formation pathways are also incorporated, in which SO_2 is oxidized by NO_2 and HONO (R27–R28).

$$SO_{2(aq)}^{T} + 2NO_{2(aq)} \rightarrow SO_4^{2-} + 2HONO_{(aq)} \quad \text{(R27)}$$

$$SO_{2(aq)}^{T} + HONO_{(aq)}^{T} \rightarrow SO_4^{2-} + 0.5N_2O_{(aq)} \quad \text{(R28)}$$

Tables 1 and 2 show all the rate constants of aqueous-phase reactions and the Henry's law constants of the reactants. The solubilities of transition metals Fe and Mn are reduced following Shao et al. (2019). Ten advected tracers are added: one is the aerosol HMS species and the others represent different sulfate formation pathways. Transport and deposition of these tracers are treated in the same way as the sulfate tracer. In addition, several other changes are made in the control simulation to the standard model. First, we update the dry deposition scheme and the reactive uptake coefficients of NO_2, NO_3, and N_2O_5 on aerosols, following Jaeglé et al. (2018) and Shah et al. (2018). Second, this simulation includes some updates developed by Luo et al. (2019, 2020) in the treatments of wet processes, allowing for spatially and temporally varying in-cloud condensation water contents, empirical washout rates for water-soluble aerosols and nitric acid, the cloud fraction available for aqueous chemistry, and rainout efficiencies for water-soluble aerosols and gases. Third, more ions are included in the cloud water pH calculation. We consider Ca^{2+}, Mg^{2+}, NH_4^+, Na^+, H^+, OH^-, Cl^-, SO_4^{2-}, NO_3^-, NO_2^-, HSO_3^-, SO_3^{2-}, HCO_3^-, CO_3^{2-}, $HCOO^-$, CH_3COO^-, HMS, and $CH_3SO_3^-$. The Newton-Raphson method is used to find the solution to the cubic electroneutrality equation (Luo et al., 2020). Ca^{2+} and Mg^{2+} are assumed to constitute 3% and 0.6%, respectively, of the dust by mass (Claquin et al., 1999; Fairlie et al., 2010; Nickovic et al., 2012; Shao et al., 2019). Only Na^+ and Cl^- from sea-salt aerosols are considered. HMS and $CH_3SO_3^-$ are from the cloud scavenging of aerosols. NO_2^-, $HCOO^-$, and CH_3COO^- are from the scavenging of HONO, HCOOH, and CH_3COOH, respectively. Fourth, HMS, $CH_3SO_3^-$, and Ca^{2+} and Mg^{2+} in fine dust are included in the ISORROPIA calculations. We assume the same hygroscopicity of HMS and MSA as sulfate (Xu et al., 2020).

We evaluate the performance of the control simulation by comparing it with the standard GEOS-Chem v12.1.0 (GC12.1.0). Figure S1 shows the horizontal distributions of surface SO_4^{2-} and SO_2 concentrations. The global average SO_4^{2-} in the control simulation is reduced by 24% compared to GC12.1.0. The updates in the treatments of wet processes by Luo et al. (2019; 2020) are primarily responsible for this difference. The SO_4^{2-} concentrations modeled in the control simulation are consistent with the improved model results in Luo et al. (2020), which have been found to agree well with SO_4^{2-} observed in the United States, Europe, and Asia (Luo et al., 2020). Moreover, since GC12.1.0 was released in late 2018, it is necessary to compare it with a more recent model version. Accordingly, we conduct a simulation using the standard GEOS-Chem v12.7.0 (GC12.7.0, released in February 2020, wiki.seas.harvard.edu/geos-chem/index.php/GEOS-Chem_12, last access: 10 June 2020). We find that the global average SO_4^{2-} in GC12.7.0 only differs little (3%) compared with that in GC12.1.0 (Fig. S2).

Below, we provide details on the calculation of cloud sulfur chemistry and highlight the need for more accurate representations of in-cloud SO_2 titration by various reactants, which include O_3 (R22), H_2O_2 (R23), O_2 (R24), HOBr (R25), NO_2 (R27), HONO (R28), and HCHO (R8). Cloud sulfur chemistry is calculated locally in the model grid cells where aqueous clouds are present. f_c (dimensionless, $0 \le f_c \le 1$) denotes the fraction of aqueous cloud in a grid cell, and L (m^3 H_2O m^{-3} air) denotes the in-cloud liquid water content. In each chemistry time step (Δt = 20 min), the losses of SO_2 in the above reactions (R8, R22–R25, R27–R28) are calculated. R24 is treated as a first-order reaction of SO_2 (O_2 is in large excess), while the other reactions are second

Deleted: aqueous-phase reaction

Deleted: reactants'

order. The first- and second-order rate constants for the aqueous reaction of $SO_{2(aq)}^{T}$ and $X_{i(aq)}$, $k_{1,aq,i}$ (s^{-1}) and $k_{2,aq,i}$ ($M^{-1}\ s^{-1}$), are obtained by Eq. 10 from the kinetic data in Table 1. X_i (i = 1:7) represents the i^{th} reactant with SO_2. $R_{aq,i}$ is the reaction rate ($M\ s^{-1}$). $k_{1,aq,i}$ and $k_{2,aq,i}$ are used to derive the first- and second-order rate constants for the heterogeneous reaction of $SO_{2(g)}$ and $X_{i(g)}$, $k_{1,g,i}$ (s^{-1}) and $k_{2,g,i}$ (mol $mol^{-1}\ s^{-1}$) (Eq. 11). H_{SO2}^{*} and H_{Xi} indicate their Henry's law constants. $f_{g,SO2}$ and $f_{g,Xi}$ are the gas-phase partitioning fractions of SO_2 and X_i, respectively (Eq. 12). R is the gas constant. T (K) is the temperature. P (atm) is atmospheric pressure. The loss of SO_2 over time Δt, $\Delta SO_{2_{g,i}}$, is solved analytically (Eq. 13). $\left[SO_{2,t=0}\right]_g$ and $\left[X_{i,t=0}\right]_g$ are the mixing ratios (mol mol^{-1}) for $SO_{2(g)}$ and $X_{i(g)}$ at the beginning of this time step. The grid-average losses of $SO_{2(g)}$ from all seven reactions are limited by the availability of $SO_{2(g)}$ within the cloud fraction f_c.

$$k_{1,aq,i} = R_{aq,i}/\left[SO_2^T\right]_{aq} \text{ and } k_{2,aq,i} = R_{aq,i}/\left(\left[SO_2^T\right]_{aq}[X_i]_{aq}\right) \quad (10)$$

$$k_{1,g,i} = k_{1,aq,i}H_{SO2}^{*}f_{g,SO2}LRT \text{ and } k_{2,g,i} = k_{2,aq,i}H_{SO2}^{*}f_{g,SO2}H_{Xi}f_{g,Xi}PLRT \quad (11)$$

$$f_{g,SO2} = \left(1 + H_{SO2}^{*}LRT\right)^{-1} \text{ and } f_{g,Xi} = (1 + H_{Xi}LRT)^{-1} \quad (12)$$

$$\Delta SO_{2_{g,i}} = \begin{cases} \left[SO_{2,t=0}\right]_g\left[1 - \exp\left(-k_{1,g,i}\Delta t\right)\right], 1^{st} \text{ order} \\ \dfrac{\left[SO_{2,t=0}\right]_g\left[X_{i,t=0}\right]_g(C-1)}{\left[SO_{2,t=0}\right]_g C - \left[X_{i,t=0}\right]_g}, C = \exp\left[\left(\left[SO_{2,t=0}\right]_g - \left[X_{i,t=0}\right]_g\right)k_{2,g,i}\Delta t\right], 2^{nd} \text{ order} \end{cases} \quad (13)$$

Since multiple in-cloud reactions consume SO_2 simultaneously, it is important to allow them to compete effectively and fairly. As shown in Eq. 13, the contribution of the i^{th} reaction to the total $SO_{2(g)}$ loss depends on its rate constant ($k_{1,g,i}$ or $k_{2,g,i}$), its relative abundance ($\left[X_{i,t=0}\right]_g/\left[SO_{2,t=0}\right]_g$), and the choice of Δt. Ideally, Δt should be smaller than the lifetime (τ_i) of $SO_{2(g)}$ for any i^{th} reaction. τ_i is the inverse of the pseudo-first-order rate constant, $\tilde{k_{1,g,i}}$, which equals to $k_{1,g,i}$ for a first-order reaction and to $k_{2,g,i}\left[X_{i,t=0}\right]_g$ for a second-order reaction. Figure 3 shows the probability density distributions of the calculated $\tilde{k_{1,g,i}}$ and the total rate constant for the seven reactions, $\sum_{i=1}^{7}\tilde{k_{1,g,i}}$, in the lower troposphere for a randomly selected week in boreal summer. $\tilde{k_{1,g,i}}$ (and thus τ_i) can vary by several orders of magnitude in different model grid cells. Notably, there is a > 50% possibility that the lifetime of $SO_{2(g)}$ is smaller than 20 min, the Δt used in this simulation. The rapid consumption of $SO_{2(g)}$ is mainly via O_3 and H_2O_2, as shown in Fig. 3 and Table S1 (statistics of probability distributions). The other five reactions consuming SO_2 (HCHO, TMI+O_2, NO_2, HONO, and HOBr) can be considered as minor pathways. This means that using Δt =20 min for the sulfur chemistry will in general lead to an underestimation of the contribution of O_3 and H_2O_2 and an overestimation of the importance of the other reactants such as HCHO. An example is provided in Text S1 to conceptually explain the effect of Δt on the competition of different reactions. We conduct a sensitivity simulation in which Δt is set to 10 min and, as we expect, the SO_4^{2-} concentrations through the cloud O_3 chemistry increase significantly (Fig. S3). A simple way to solve this problem

Formatted: Subscript

Formatted: Subscript

Formatted: Subscript

is to reduce Δt. The possibility of $\tau < \Delta t$ decreases to only 4% when Δt = 1 min (Fig. 3 and Table S1). Also, most (> 80%) of the cases of τ < 1 min arise from the rapid reaction of SO_3^{2-} with $O_{3(aq)}$ when cloud water pH is high. The remaining cases are from the reactions of SO_3^{2-} with $HOBr_{(aq)}$ and $HCHO_{(aq)}$. The other four reactions can hardly lead to τ < 1 min. We change the time step to 1 min when calculating in-cloud SO_2 titration in the default simulation (Sect. 2.5).

Another issue in the control simulation is, in a partly cloudy ($0 < f_c < 1$) model grid, that the mixing of air between the cloudy fraction (f_c) and the cloud free fraction ($1-f_c$) occurs in the same timescale as the chemistry time step of the model (Holmes et al., 2019). In each time step, the grid-average loss of $SO_{2(g)}$ from all in-cloud reactions cannot exceed the amount of $SO_{2(g)}$ available within the cloudy fraction and at the beginning of this time step (Eq. 14). This so-called "cloud partitioning method" is unphysical as the entrainment/detrainment rates are affected by the setting of the chemistry time step (Holmes et al., 2019). Since many chemical transport models such as GEOS-Chem do not resolve individual clouds, Holmes et al. (2019) developed a more realistic and stable "entrainment-limited uptake" method, which accounts for cloud entrainment/detrainment within the chemical rate expression. We apply this method to the default simulation (Sect. 2.5).

$$\sum_{i=1}^{7} \Delta SO_{2g,i} \le f_c \left[SO_{2,t=0}\right]_g \quad (14)$$

2.5 Default simulation

Three major changes are made in this simulation based on the control simulation, as mentioned in Sect. 2.4. The first is applying the "entrainment-limited uptake" method developed by Holmes et al. (2019) to more realistically model the entrainments and detrainments of air in cloudy grid cells. The second is reducing the time step to 1 min when calculating cloud sulfur reactions to better quantify the competition of different chemical pathways consuming SO_2. The third is adding the reaction of H_2O_2 and SO_2 in aerosol water using the kinetic data reported recently by Liu et al. (2020). The control simulation only includes the reaction of H_2O_2 and SO_2 in cloud water. Figure S4 shows the horizontal distributions of surface SO_4^{2-} and SO_2 concentrations in the control and default simulations, and only very small differences (4% for SO_4^{2-} and 1% for SO_2) are found for their global average values.

Deleted: new

Deleted: from

In the "entrainment-limited uptake method" (Holmes et al., 2019), the first-order loss rate of $SO_{2(g)}$ in a model grid cell due to heterogeneous cloud chemistry, k_1 (s^{-1}), depends on the cloud fraction (f_c), the detrainment rate (k_c, s^{-1}), and the in-cloud total pseudo-first-order rate constant, $k^*_{1,g} = \sum_{i=1}^{7} k^*_{1,g,i}$ (s^{-1}) (Eq. 15). As shown in Holmes et al. (2019), the entrainment/detrainment (k_c term) limits its reactive uptake. In a completely cloudy condition (f_c = 1), Eq. 15 reduces to $k_1 = \sum_{i=1}^{7} k^*_{1,g,i}$. k_c is the reverse of the in-cloud residence time of air (τ_c), which varies with cloud types and ranges from 15 to 120 min for stratus and cumulus

clouds (Holmes et al., 2019). We use τ_c = 30 min in this work since MERRA-2 does not provide this information. A sensitivity simulation shows that assuming a τ_c of 60 min decreases the global average surface SO_4^{2-} concentration by 10%. Holmes et al. (2019) have pointed out that future studies are needed to specify the spatiotemporal variability of τ_c in the global reanalysis datasets. Within the cloudy fraction of a model grid cell, as shown in Fig. 1 and Eq. 16, the heterogeneous reaction rates are limited by a series of resistances associated with the mass transfer processes from the gas phase to the aqueous phase, including gas-phase diffusion, transfer of the reactants across the air–water interface, and aqueous-phase diffusion (Ravishankara, 1997; Jacob, 2000). In Eq. 16, the α_{SO2} term represents the limitation due to mass accommodation at the air–water interface and the $D_{g,SO2}$ term represents that due to gas-phase diffusion. A dimensionless parameter Q, whose expression is given by Eq. 17 (0 < Q < 1), is used to account for aqueous-phase mass transport limitations when calculating $k_{1,aq,i}$ and $k_{2,aq,i}$ (Eq. 10).

$$\frac{1}{k_1} = \frac{1-f_c}{f_c k_c} + \frac{1}{f_c k_{1,g}^*} = \frac{1-f_c}{f_c k_c} + \frac{1}{f_c \sum_{i=1}^{7} k_{1,g,i}^*} \tag{15}$$

$$\frac{1}{k_{1,g,i}^*} = \frac{1}{\tilde{k}_{1,g,i}} + \frac{4}{A v_{SO2} \alpha_{SO2}} + \frac{r}{A D_{g,SO2}} \tag{16}$$

$$Q = 3\left(\frac{\coth q}{q} - \frac{1}{q^2}\right), \quad q = r\sqrt{\frac{\sum_{i=1}^{7} \tilde{k}_{1,aq,i}}{D_{aq}}} \tag{17}$$

Here, r is the radius of cloud droplets and is assumed to be 10^{-5} m. A (m^2 m^{-3} air) is the surface area density of cloud droplets and is derived using L and r. v_{SO2} (m s^{-1}) is the molecular mean speed of SO_2 (Eq. 18). α_{SO2} (dimensionless) is the mass accommodation coefficient of SO_2 (Table 3). $D_{g,SO2}$ (m^2 s^{-1}) is the gas-phase diffusion coefficient of SO_2 (Eq. 19). q is a dimensionless parameter determined by r, D_{aq}, and $\tilde{k}_{1,aq,i}$ (the pseudo-first-order rate constant with respect to $SO_{2(aq)}^T$ for the i^{th} reaction). For a first-order and second-order reaction, $\tilde{k}_{1,aq,i}$ is equal to $k_{1,aq,i}$ and $k_{2,aq,i}[X_i]_{aq}$, respectively (Eq. 10). D_{aq} is the aqueous-phase diffusion coefficient (10^{-9} m^2 s^{-1}) (Song et al., 2019a). M_{SO2} (g mol^{-1}) represents the molar mass of SO_2. $\rho_{n,air}$ (molecule cm^{-3}) is the number density of air. $\tilde{k}_{1,g,i}$ (s^{-1}) is the pseudo-first-order rate constant with respect to $SO_{2(g)}$ for the i^{th} aqueous-phase reaction, and equals to $k_{1,g,i}$ and $k_{2,g,i}[X_i]_g$ for the first-order and second-order reactions, respectively. In addition, as illustrated in Fig. 1, the second-order reaction rate may also be limited by the mass transfer of X_i. Thus, the in-cloud pseudo-second-order rate constant, $k_{2,g,i}^*$, is given by Eq. 20. v_{Xi}, α_{Xi}, and $D_{g,Xi}$ are the molecular mean speed, the mass accommodation coefficient, and the gas-phase diffusion coefficient of X_i, respectively. v_{Xi} and $D_{g,Xi}$ are calculated similarly to Eqs. 18 and 19. α_{Xi} can be found in Table 3.

$$v_{SO2} = \sqrt{8RT/(\pi M_{SO2})} \tag{18}$$

$$D_{g,SO2} = \frac{9.45 \times 10^{13} \times \sqrt{T \times (3.47 \times 10^{-2} + 1/M_{SO2})}}{\rho_{n,air}} \quad (19)$$

$$\frac{1}{k^*_{2,g,i}} = \frac{1}{k_{2,g,i}} + \mathrm{MAX}\left(\frac{4[X_i]_g}{A v_{SO2} \alpha_{SO2}} + \frac{r[X_i]_g}{A D_{g,SO2}}, \frac{4[SO_2]_g}{A v_{Xi} \alpha_{Xi}} + \frac{r[SO_2]_g}{A D_{g,Xi}}\right) \quad (20)$$

As mentioned in Sect. 2.4, we do not change the chemistry time step of the model (Δt = 20 min) but only the time step (to 1 min) when identifying cloud SO_2 reactions. For each 1-min time step, the loss of $SO_{2(g)}$ for the i^{th} reaction, $\Delta SO_{2g,i}$, is solved analytically using Eq. 13, in which $k_{1,g,i}$ and $k_{2,g,i}$ are replaced by $k^*_{1,g,i}$ from Eq. 16 and $k^*_{2,g,i}$ from Eq. 20, respectively. This change reflects the mass transport limitations. The grid-average first-order loss rate of $SO_{2(g)}$, k_1, is calculated using Eq. 15, in which $\sum_{i=1}^{7} k^*_{1,g,i}$ is replaced by the in-cloud total pseudo-first-order rate constant estimated from $\sum_{i=1}^{7} \Delta SO_{2g,i}$. The grid-average loss of $SO_{2(g)}$ and the contributions of different reactions are calculated then using k_1 and $\Delta SO_{2g,i}$. The mixing ratios of the relevant chemical species are updated at the end of this 1-min time step and used as initial condition for the next time step. The calculations are repeated 20 times in a chemistry time step.

The cloud water pH and rate constants for the heterogeneous reaction of $SO_{2(g)}$ and $X_{i(g)}$ are calculated only at the beginning of each chemistry time step. We conduct a sensitivity simulation that redoes cloud SO_2 calculations using the cloud water pH and rate constants estimated at the end of each chemistry time step. The resulting change is insignificant (global mean SO_4^{2-} concentration decreases by < 2%). The aqueous-phase sulfur reactions are hard-coded into the model. Ideally, further model development of cloud chemistry should apply the advanced numerical solvers generated by the Kinetic PreProcessor (KPP), which may not only allow a full coupling of gas-phase and cloud chemistry but also make it easier for the model to incorporate additional aqueous reactions (Fahey et al., 2017; Personal communication, Viral Shah, 18 December 2019).

The implementation of sulfur chemistry in aerosol water is similar to that for cloud sulfur chemistry. As shown in Fig. 1, the heterogeneous reaction rates are also controlled by the mass transfer of reactants from the gas to the aqueous phase. The difference is that aerosols (and aerosol water) can be considered evenly distributed in a model grid cell, and it is unnecessary to include the entrainment/detrainment processes. The major difficulty in parameterizing the aerosol water sulfur chemistry is the lack of suitable reaction rate constants. Liu et al. (2020) have recently found that the high ionic strength of deliquesced aerosols significantly enhances the rate constants for the reaction of H_2O_2 and SO_2. The enhancement factor (EF) relative to its rate constant in dilute solutions is derived by fitting the data in Liu et al. (2020) as a function of the molality-based ionic strength, μ_b (mol kg^{-1}) (Table 1). The water content, pH, μ_b, and the absorbed water volume fraction of inorganic aerosols are

calculated by the ISORROPIA II model (Sect. 2.2). The aerosol water volume fraction of 0.25 is used as a threshold for the occurrence of aqueous reactions as it governs the transition of aerosols to a liquid state (Bateman et al., 2016).

2.6 Sensitivity simulations

In addition to the control and default simulations, we conduct ten sensitivity simulations to investigate the key factors leading to uncertainty in the modeled HMS concentrations. As shown in Table 4, all these sensitivity simulations are based on the default simulation. HiKf, HiKd, and HiOH make changes to HMS formation, decomposition, and oxidation, respectively, in heterogeneous cloud chemistry. HiKf uses the high k_f instead of the low k_f in the default simulation (Sect. 2.1.1). HiKd increases k_d by a factor of 2, the upper limit of its estimate (Sect. 2.1.2). HiOH increases $[OH]_{aq}$ by a factor of 10, matching its average value in current multiphase models (Sect. 2.1.3). CWpH considers less ions, i.e., NH_4^+, H^+, OH^-, SO_4^{2-}, NO_3^-, HSO_3^-, SO_3^{2-}, HCO_3^-, CO_3^{2-}, HMS, and $CH_3SO_3^-$, in cloud water pH calculations.

AWOH, AWK0, and AWKE examine the potential role of aerosol water in heterogeneous HMS chemistry (Table 4). Since the rate constants of HMS chemical reactions in concentrated solutions have not been determined experimentally, we have to make assumptions about these data. AWOH implements the oxidation of HMS by OH in aerosol water and assumes the same rate constant as those for cloud water. AWK0 adds the formation and decomposition of HMS in aerosol water also using the rate constants for cloud water. Theoretically, we anticipate that the rate constant of HMS formation, k_f, in concentrated solutions should be enhanced relative to dilute solutions (Song et al., 2019a), similar to the situation found for the reaction of H_2O_2 and SO_2. AWKE arbitrarily increases k_f by the same EF for the H_2O_2 and SO_2 reaction (Table 1). The implementation of the above chemical reactions of HMS in aerosol water follows the approach described in Sect. 2.5.

Three sensitivity simulations, HiNH3, HiFA, and AppHet, focus on East Asia (Table 4). SO_2, HCHO, and NH_3 emissions may influence the modeled HMS. Recent studies have shown, although SO_2 emissions are well understood, that there may be large uncertainties in emissions of NH_3 and HCHO in China (Pan et al., 2018; Kong et al., 2019; Liu et al., 2019; Song et al., 2019a). An inverse study found that the MEIC inventory underestimated NH_3 emissions by 30% nationally and by > 40% in eastern and central regions using observations over the same time period as our study (Kong et al., 2019). HiNH3 increases the anthropogenic emissions of NH_3 in MEIC by 50%. Less information is available regarding the emissions of HCHO due to its sparse observations and complex chemistry. Model–observation comparisons in Beijing suggested a strong underestimation of HCHO emissions during winter (Song et al., 2019a). Mobile and residential emission sources may be responsible for its underestimation (Jaeglé et al., 2018; Song et al., 2019a). HiFA increases HCHO emissions from the transportation and residential sectors by a factor of 5. Chemical transport models commonly underestimate SO_4^{2-} during winter haze episodes in China, and thus some studies have adopted an apparent heterogeneous parameterization for SO_2 reactive uptake in order to compensate for the missing SO_4^{2-} (Zheng et al., 2015; Cheng et al., 2016; Wang et al., 2016; Liu et al., 2019; Li et al., 2020).

This parameterization is applied in AppHet during the cold season, in which the reactive uptake coefficient of SO_2 increases from 2×10^{-5} to 5×10^{-5} with $50\% < RH \leq 100\%$ (Zheng et al., 2015).

3 Results and discussion

3.1 Spatial and seasonal distributions in the default simulation

The horizontal distributions of HMS concentration in the surface layer and the vertical profiles of its zonal average are shown in Fig. 4 (DJF: December–January–February and JJA: June–July–August) and Fig. S5 (MAM: March–April–May and SON: September–October–November). The concentration unit is μg sm^{-3}, where 1 sm^3 equals 1 m^3 at standard temperature and pressure (273.15 K and 1013.25 hPa). The molar ratio of HMS to sulfate, also shown in Fig. 4 and Fig. S5, is a useful metric to assess the significance of HMS in sulfur chemistry. Higher HMS concentrations and HMS/sulfate ratios are found over the continental regions in the Northern Hemisphere. The vertical profiles indicate that most HMS exists in the lower troposphere. These features are expected because the precursors of HMS, SO_2 and HCHO, are more abundant in these regions compared with elsewhere (Fig. S6).

The surface HMS concentrations and HMS/sulfate molar ratios exhibit distinct seasonal patterns with maxima in DJF (boreal winter) and minima in JJA (boreal summer), and thus our analyses focus on these two seasons. It is noted that there are hotspots of HMS in JJA in Siberia that are linked to massive forest fires in that region in July 2016 (Sitnov et al., 2017). As highlighted in Fig. 4, three regions with relatively high HMS levels, East Asia (EA), Europe (EU), and North America (NA), are selected for quantitative analysis. Figure 5 shows the statistics of HMS levels from the default simulation with comparisons to other simulations. The average HMS concentrations in DJF (JJA) are 0.59 (0.09), 0.16 (0.013), 0.055 (0.015) μg sm^{-3}, for EA, EU, and NA, respectively. The average HMS/sulfate ratios in DJF (JJA) are 0.09 (0.01), 0.06 (0.006), 0.04 (0.009), for EA, EU, and NA, respectively. The wintertime East Asia, northern China in particular, has both the highest HMS concentration and highest HMS/sulfate ratio. The average HMS concentrations (1–3 μg sm^{-3}) and HMS/sulfate ratios (0.1–0.2) are found during the winter season in northern China (Fig. S7).

As mentioned in Sect. 1, previous studies have suggested that the formation and existence of HMS in the condensed phase are favored generally under the following conditions: high precursor (SO_2 and HCHO) concentrations, low photochemical oxidant levels, low temperature, abundant aqueous water, and moderate acidity (Munger et al., 1984, 1986; Moch et al., 2018; Song et al., 2019a; Ma et al., 2020). The seasonal variability of HMS does not follow that of the precursor levels (Fig. S6). The seasonal variation of the geometric mean of the two precursors, $\sqrt{SO_2 \times HCHO}$, is weak because of their opposite seasonality (more SO_2 but less HCHO in winter). The cloud liquid water content (L) in the lower troposphere shows a spatial distribution with higher values over the ocean and lower values over land (Fig. S8). There is no consistent seasonal pattern of L between DJF and JJA over the three regions (EA, EU, and NA). The modeled cloud water pH exhibits a seasonal difference. The average pH in DJF

(JJA) is 4.3 (5.8), 4.7 (5.6), and 4.7 (5.7) for EA, EU, and NA, respectively. The higher pH in JJA is related to more abundant gaseous NH_3 (Fig. S8), given the buffer capacity of NH_3 in moderating the acidity of atmospheric condensed water (Song et al., 2019b).

One of the above-mentioned factors favoring HMS is the moderate acidity. This term is somewhat ambiguous but is used to represent the pH range that allows for relatively rapid formation and slow decomposition of HMS. We show in Fig. 2 that both k_f and k_d increase with pH. The lifetime of HMS with respect to decomposition is about 60, 6, and 0.6 hours at pH 5, 6, and 7, respectively, at 298 K, and is even larger at lower T. For the range of pH in the three regions (its average from 4.3 to 5.8), the decomposition of HMS is so slow that its chemical equilibrium is difficult to achieve. Accordingly, the modeled HMS levels are predominantly controlled by formation kinetics. This is supported by the results from the HiKd simulation, in which $k_d \times 2$ makes little difference in the modeled HMS compared to the default simulation (Fig. 5). The higher cloud pH in JJA should lead to faster HMS formation rates than those in DJF. However, in the default simulation, the modeled HMS levels show an opposite pattern. This is believed to be linked to the different photochemical oxidizing abilities in the two seasons. Globally, the two main aqueous oxidants for SO_2 are O_3 and H_2O_2, which compete with HCHO. The competition of different pathways can be influenced by the levels of these gases, T (changing gas solubilities and rate constants), and pH (changing rate constants). O_3, H_2O_2, and HCHO all have higher concentrations in JJA (Fig. S6). The lower T in DJF favors the H_2O_2 reaction most and the O_3 reaction least. Notably, the response of the O_3 reaction to pH is essentially the same as that for HCHO since both react rapidly with SO_3^{2-}. The HCHO + SO_2 reaction is significant only when the two photochemical oxidants are inefficient.

3.2 Difference between the default and control simulations

Compared with the default simulation, the control simulation realizes very different spatial and seasonal distributions of HMS concentrations and HMS/sulfate molar ratios (Fig. S9). Figure 6 shows the differences in surface HMS concentrations for DJF and JJA. The corresponding information for MAM and SON is presented in Fig. S10. Two features are evident. First, a weak seasonality is found for the control simulation, but for the default simulation, HMS is much more abundant in DJF. Second, the control simulation predicts significantly higher HMS concentrations almost everywhere except in parts of East Asia and Europe in DJF. Interestingly, the only region where the default simulation gives higher HMS concentrations is wintertime in northern China, the focus of several studies (Moch et al., 2018; Song et al., 2019a; Ma et al., 2020). Specifically, as shown in Fig. 5, the average HMS concentrations modeled by the control simulation in DJF (JJA) are 0.60 (0.70), 0.22 (0.12), 0.14 (0.11) μg sm^{-3}, respectively, for East Asia (EA), Europe (EU), and North America (NA). The average HMS/sulfate ratios inferred from the control simulation in DJF (JJA) are 0.09 (0.14), 0.08 (0.06), 0.09 (0.07), respectively, for EA, EU, and NA.

As described in Sect. 2.5, based on the control, the default simulation improves the representations of heterogeneous cloud sulfur chemistry in the model by applying the "entrainment-limited uptake" method from Holmes et al. (2019) and by reducing the time step when calculating aqueous sulfur reactions. These changes allow for a more realistic simulation of entrainments

and detrainments of air in partly cloudy grid cells and for an effective competition of different aqueous reactions consuming SO_2. In the control simulation, the time step for calculating in-cloud sulfur reactions is the same as the chemistry time step of the model, Δt = 20 min. But there may be a > 50% possibility that the lifetime of in-cloud SO_2 is less than this Δt, as shown in Fig. 3 and described in Sect. 2.4. Given that the main reactants with in-cloud SO_2 are O_3 and H_2O_2, this setting leads to a general underestimation of the contribution of O_3 and H_2O_2 and an overestimation of importance of the minor reactants such as HCHO. The bias is larger in JJA than in DJF, as suggested by the probability distribution statistics for the in-cloud lifetime of SO_2 (Table S1).

3.3 Key uncertain factors

Section 2.6 and Table 4 describe the ten sensitivity simulations we conduct with an aim to find out the key parameters and processes leading to HMS modeling uncertainties. All of these simulations are modified based on the default simulation and can be classified into three groups: heterogeneous cloud chemistry (HiKf, HiKd, HiOH, and CWpH); heterogeneous aerosol water chemistry (AWOH, AWK0, and AWKE); and East Asia only (HiNH3, HiFA, and AppHet). A comparison of the surface HMS concentrations and HMS/sulfate molar ratios from these sensitivity simulations is provided in Fig. 5, focusing on three regions (EA, EU, and NA) and two seasons (DJF and JJA).

First, we examine the sensitivity simulations in terms of the formulation of heterogeneous cloud chemistry. HiKf, HiKd, HiOH, and CWpH make changes in HMS formation, decomposition, oxidation, and cloud water pH calculations, respectively. The surface HMS concentrations and HMS/sulfate ratios in the latter three indicate relative differences of less than ±20% compared to the default simulation. However, HiKf shows a very large increase, by a factor of 2 to 6, in modeled HMS. This is expected since the high and low k_f differ by a factor of about 3 at pH < 2 and by a factor of about 6 at pH > 4 (Sect. 2.1.1). As described in Sect. 2.1.3, the formation of HMS and its oxidation by OH represent an indirect oxidation pathway for SO_2. The sulfate yield, defined as the number of SO_4^{2-} ions produced due to each attack of OH on HMS, is set to 2 in our simulations. The small difference between the HiOH and default simulations suggests that this indirect pathway should be insignificant.

Second, three sensitivity simulations are conducted for East Asia, as it is found most suitable for the existence of HMS. HiNH3 and HiFA increase the concentrations for modeled HMS in DJF by 60% and 20%, respectively, whereas the concentrations by AppHet are decreased by about 30%. The changes due to HiNH3 and HiFA are much smaller in JJA (Fig. 5). The increase of HMS in HiNH3 can be attributed to higher cloud water pH, and its decrease in AppHet should be related to a decrease in SO_2 available for cloud chemistry. Interestingly, HiNH3 increases the HMS/sulfate ratios in DJF by only 20%. The higher cloud water pH enhances the formation of sulfate through the pH-sensitive pathways such as the reaction of SO_2 with O_3.

Third, AWOH, AWK0, and AWKE explore the potential role of heterogeneous aerosol water HMS chemistry. The challenge of modeling aerosol water HMS chemistry is the lack of its reaction rate constants in concentrated aqueous solutions. We use

the rate constants from dilute solutions in AWOH and AWK0. The oxidation of HMS by OH in aerosol water leads to losses of 10–20% (DJF) and 40–60% (JJA) (Fig. 5). The formation and decomposition of HMS in aerosol water result in negligible changes in the modeled HMS concentrations, as shown in Fig. 7 (DJF) and Fig. S11 (the other seasons). Results from AWKE suggest that aerosol water might play a role in the formation of HMS only when the k_f is strongly enhanced in concentrated solutions like the rate constant of the SO_2 reaction with H_2O_2.

Overall, our sensitivity simulations suggest that the key uncertain parameter in the model is k_f. Based on existing experimental results, the low value for k_f is most reasonable (Sect. 2.1.1), but we cannot rule out the possibility of higher values. The key uncertain process is modeling the aerosol water chemistry of HMS in the absence of reliably defined rate constants.

3.4 Comparison with observations

The observations of HMS in ambient aerosols are sparse and we provide here a comparison between the available observations and two model simulations (control and default) in Table 5. Since these observations have been collected over the past three decades while our simulations cover only one year, it is more appropriate to use the molar ratios of HMS/SO_4^{2-} or HMS/MSA rather than absolute HMS concentrations. The measurement techniques of HMS in different studies have been different (Table 5) and their effects on the reported results are unclear. Among the observations shown in Table 5, the highest HMS/SO_4^{2-} ratio of 11% has been found in winter in Beijing by Ma et al. (2020). Model results from both default and control simulations agree well with this observed ratio. Less HMS was observed in other regions, including New Mexico (USA), Germany, and Osaka Bay (Japan). The default simulation overestimates the HMS/SO_4^{2-} or HMS/MSA ratios by a factor of 2–3, whereas the control simulation overestimates these ratios by an order of magnitude. Given the various sources of uncertainty in the model and the mismatches between the observations and global simulations, we conclude that the default simulation reasonably reproduces the available HMS observations in different regions.

A more detailed comparison of the model with observations in Beijing is provided below. The observations in Ma et al. (2020) cover 73 days in winter and 11 polluted days in other seasons. The data for the other seasons is presented only in their discussion paper. Because of the coarse resolution of global model, we do not expect our simulations to capture the day-to-day variability that is observed at a single site. Accordingly, we examine the ability of our simulations to reproduce the observed relationships between HMS and its influencing factors. Figure 8 provides scatter plots of HMS concentrations (and HMS/SO_4^{2-} ratios) versus two variables (O_3 and RH) and compares the data from observations and model simulations (control and default). The level of O_3 represents photochemical oxidizing capacity and RH may indicate the abundance of aqueous water in the lower troposphere.

We find a similar relationship between HMS and O_3 from the observations and default simulation (Fig. 8). Significant HMS levels are observed and modeled only under low O_3 conditions (< 20 ppb). However, the control simulation obtains another cluster of days with high HMS levels when O_3 is abundant (> 40 ppb). This cluster is linked to the inappropriate representation

of heterogeneous cloud sulfur chemistry in the control simulation. The large time step for SO_2 titration excessively favors the reaction of SO_2 with HCHO, as described in Sect. 2.4 and Fig. 3. It should be noted in Ma et al. (2020) that only 11 daily samples had O_3 levels larger than 20 ppb. There might be a possibility that the days with high levels of both HMS and O_3 were missed in their sampling coverage, but we think it is unlikely given the rapid oxidation of SO_2 by the photochemical oxidants (gaseous OH and aqueous O_3 and H_2O_2) under such conditions.

The scatter plots of HMS and RH show a similar exponential-like relationship in the observations and model simulations (Fig. 8). Such an exponential-like relationship has been interpreted to support the hypothesis that HMS is produced through aerosol water (Song et al., 2019a; Ma et al., 2020). This is because the amount of aerosol water also exhibits an exponential relationship with RH (Song et al., 2018, 2019b). Interestingly, our model simulations using aqueous clouds as the only medium can obtain a similar relationship between HMS and RH, which reduces the credibility of this aerosol water hypothesis. Global atmospheric models, including the numerical weather prediction model employed in the MERRA-2 reanalysis, are usually not capable of resolving sub-grid cloud processes, and cloud properties are parameterized using an RH-related statistical scheme (Molod, 2012; Molod et al., 2015). Thus, it is not surprising to find a relationship between RH and HMS in the simulations.

3.5 Knowledge gained and remaining gaps

The different spatiotemporal patterns of the HMS levels modeled by the control and default simulations indicate the importance of an appropriate representation of heterogeneous cloud sulfur chemistry. The default simulation better reproduces the limited available observations of HMS in different regions of the world. Our modeling suggests that photochemical oxidizing capacity is a key influencing factor for HMS formation because it affects the competition of HCHO with oxidants (e.g., O_3 and H_2O_2) for SO_2. This factor is partly responsible for the distinct seasonality in HMS modeled by the default simulation. On a regional scale, the most suitable place for the formation and existence of HMS is parts of East Asia in the lower troposphere during the cold season. Aqueous clouds are the major medium for HMS chemistry since the model simulations can reasonably reproduce both the observed HMS levels and the relationship between in situ HMS and RH when assuming this as the only medium. Aerosol water may play a role if the rate constant of HMS formation is greatly enhanced in concentrated solutions. This finding is consistent with several studies (Jacob, 1986; Olson and Hoffmann, 1989; Whiteaker and Prather, 2003; Moch et al., 2018). The observations of HMS are sparse, and more data are required to validate the model. The quantification of HMS in different seasons and over different photochemical conditions is particularly valuable.

Two knowledge gaps are identified from our sensitivity simulations. First, the key uncertain factor in the model is k_f, the rate constant for HMS formation. Large discrepancies exist among existing laboratory experiments (Fig. 2), and future laboratory studies are required to narrow its uncertainty. Second, the lack of kinetic and thermodynamic data for HMS chemistry in concentrated solutions poses a key challenge to modeling HMS processing in aerosol water, and new laboratory studies are needed. Also, we did not consider the uncertainty in the meteorological reanalysis. It is unknown whether the model results

are sensitive to cloud distributions and properties. Although MERRA-2 assimilates extensive observations and represents the atmospheric states accurately, cloud properties are modeled exclusively. Studies have shown biases in seasonal and spatial variations of cloudiness when comparing the reanalysis data with lidar and satellite observations (Kennedy et al., 2011; Stengel et al., 2018; Miao et al., 2019).

Recently, the quantum chemical calculations by Chen and Zhao (2020) suggested that hydroxymethyl sulfite (HMSi), an isomer of HMS, might also be produced by an aqueous reaction of HCHO and SO_2. The laboratory experiments of De Haan et al. (2020) demonstrated that HMS was one of the major products from the aqueous processing of glyoxal monobisulfite ($CH(OH)_2CH(OH)SO_3^-$), the adduct of glyoxal and SO_2. The new mechanisms need to be considered in future model studies.

4 Conclusion

Based on appropriate implementation of heterogeneous HMS chemistry and assuming aqueous clouds as the only medium, the global GEOS-Chem model can reasonably reproduce the limited available observations of HMS among different regions. The modeled HMS concentrations and HMS/sulfate ratios show a clear seasonal pattern with higher values in the cold period. The spatial distributions of HMS in descending order are East Asia, Europe, and North America. Our model simulations find the highest average HMS concentrations (1–3 μg m^{-3}) and HMS/sulfate molar ratios (0.1–0.2) in northern China during the winter season. Photochemical oxidizing capacity affects the competition of HCHO with oxidants (e.g., O_3 and H_2O_2) for SO_2, and is a key factor influencing HMS formation. Aqueous clouds act as the primary medium for HMS chemistry while aerosol liquid water could play a role if the rate constant for HMS formation is greatly enhanced.

This study identifies future research needs. Laboratory experiments should reduce the uncertainty in the formation rate constant of HMS and determine the kinetics for HMS chemistry in concentrated solutions. More field observations of HMS, especially its quantification in different seasons and photochemical conditions, are helpful to validate the model. The coarse resolution of the global model does not allow it to capture day-to-day observations at a single site, and we are preparing another paper to demonstrate the capacities of regional model with a finer resolution to reproduce individual haze events in northern China.

Code and Data availability. The standard GEOS-Chem model is available at: https://doi.org/10.5281/zenodo.3860693. The code changes made in this study are available at: https://github.com/shaojiesong/GC1210_sulfchem_Song2020. The laboratory and observational data used in this study are all obtained from published papers and books.

Supplement. The supplement related to this article is available online at:

Author contributions. SS initiated the study, carried out analysis, and wrote the initial draft. All authors helped interpret the data, provided feedback, and commented on the manuscript.

Competing interests. The authors declare that they have no conflict of interest.

Acknowledgements. We thank Qianjie Chen, Pingqing Fu, John Jayne, Gan Luo, J. William Munger, Chris P. Nielsen, Jingyuan Shao, Viral Shah, Xuan Wang, Yuxuan Wang, Douglas R. Worsnop, and Lin Zhang for helpful discussions.

Financial support. This work was supported by the Harvard Global Institute.

Review statement.

References

Alexander, B., Park, R. J., Jacob, D. J., Li, Q. B., Yantosca, R. M., Savarino, J., Lee, C. C. W., and Thiemens, M. H.: Sulfate formation in sea-salt aerosols: Constraints from oxygen isotopes, J. Geophys. Res. Atmos., 110, 10.1029/2004jd005659, 2005.

Alexander, B., Park, R. J., Jacob, D. J., and Gong, S.: Transition metal-catalyzed oxidation of atmospheric sulfur: Global implications for the sulfur budget, J. Geophys. Res. Atmos., 114, 10.1029/2008jd010486, 2009.

Alexander, B., Allman, D. J., Amos, H. M., Fairlie, T. D., Dachs, J., Hegg, D. A., and Sletten, R. S.: Isotopic constraints on the formation pathways of sulfate aerosol in the marine boundary layer of the subtropical northeast Atlantic Ocean, J. Geophys. Res. Atmos., 117, 10.1029/2011jd016773, 2012.

Bateman, A. P., Gong, Z., Liu, P., Sato, B., Cirino, G., Zhang, Y., Artaxo, P., Bertram, A. K., Manzi, A. O., Rizzo, L. V., Souza, R. A. F., Zaveri, R. A., and Martin, S. T.: Sub-micrometre particulate matter is primarily in liquid form over Amazon rainforest, Nat. Geosci., 9, 34-37, 10.1038/ngeo2599, 2016.

Bates, T. S., Calhoun, J. A., and Quinn, P. K.: Variations in the methanesulfonate to sulfate molar ratio in submicrometer marine aerosol particles over the south Pacific Ocean, J. Geophys. Res. Atmos., 97, 9859-9865, 10.1029/92jd00411, 1992.

Betterton, E. A., and Hoffmann, M. R.: Oxidation of aqueous sulfur dioxide by peroxymonosulfate, J. Phys. Chem., 92, 5962-5965, 1988.

Blackadder, D. A., and Hinshelwood, C.: 554. The kinetics of the decomposition of the addition compounds formed by sodium bisulphite and a series of aldehydes and ketones. Part I, Journal of the Chemical Society (Resumed), 2720-2727, 10.1039/JR9580002720, 1958.

Boniface, J., Shi, Q., Li, Y. Q., Cheung, J. L., Rattigan, O. V., Davidovits, P., Worsnop, D. R., Jayne, J. T., and Kolb, C. E.: Uptake of Gas-Phase SO_2, H_2S, and CO_2 by Aqueous Solutions, J. Phys. Chem. A, 104, 7502-7510, 10.1021/jp000479h, 2000.

Boyce, S. D., and Hoffmann, M. R.: Kinetics and mechanism of the formation of hydroxymethanesulfonic acid at low pH, J. Phys. Chem., 88, 4740-4746, 10.1021/j150664a059, 1984.

Brüggemann, M., Xu, R., Tilgner, A., Kwong, K. C., Mutzel, A., Poon, H. Y., Otto, T., Schaefer, T., Poulain, L., Chan, M. N., and Herrmann, H.: Organosulfates in Ambient Aerosol: State of Knowledge and Future Research Directions on Formation, Abundance, Fate, and Importance, Environ. Sci. Technol., 54, 3767-3782, 10.1021/acs.est.9b06751, 2020.

Chen, K., and Zhao, J.: Theoretical investigation of a potentially important formation pathway of organosulfate in atmospheric aqueous aerosols, Sci. Rep., 10, 6299, 10.1038/s41598-020-61968-2, 2020.

Chen, Q., Schmidt, J. A., Shah, V., Jaeglé, L., Sherwen, T., and Alexander, B.: Sulfate production by reactive bromine: Implications for the global sulfur and reactive bromine budgets, Geophys. Res. Lett., 44, 7069-7078, 10.1002/2017gl073812, 2017.

Chen, Q., Sherwen, T., Evans, M., and Alexander, B.: DMS oxidation and sulfur aerosol formation in the marine troposphere: a focus on reactive halogen and multiphase chemistry, Atmos. Chem. Phys., 18, 13617-13637, 10.5194/acp-18-13617-2018, 2018.

Cheng, Y., Zheng, G., Wei, C., Mu, Q., Zheng, B., Wang, Z., Gao, M., Zhang, Q., He, K., Carmichael, G., Pöschl, U., and Su, H.: Reactive nitrogen chemistry in aerosol water as a source of sulfate during haze events in China, Sci. Adv., 2, e1601530, 10.1126/sciadv.1601530, 2016.

Chin, M., Rood, R. B., Lin, S.-J., Müller, J.-F., and Thompson, A. M.: Atmospheric sulfur cycle simulated in the global model GOCART: Model description and global properties, J. Geophys. Res. Atmos., 105, 24671-24687, 10.1029/2000jd900384, 2000.

Claquin, T., Schulz, M., and Balkanski, Y.: Modeling the mineralogy of atmospheric dust sources, J. Geophys. Res. Atmos., 104, 22243-22256, 10.1029/1999jd900416, 1999.

Davidovits, P., Kolb, C. E., Williams, L. R., Jayne, J. T., and Worsnop, D. R.: Mass Accommodation and Chemical Reactions at Gas−Liquid Interfaces, Chem. Rev., 106, 1323-1354, 10.1021/cr040366k, 2006.

De Haan, D. O., Jansen, K., Rynaski, A. D., Sueme, W. R. P., Torkelson, A. K., Czer, E. T., Kim, A. K., Rafla, M. A., De Haan, A. C., and Tolbert, M. A.: Brown Carbon Production by Aqueous-Phase Interactions of Glyoxal and SO2, Environ. Sci. Technol., 54, 4781-4789, 10.1021/acs.est.9b07852, 2020.

Deister, U., Neeb, R., Helas, G., and Warneck, P.: Temperature dependence of the equilibrium $CH_2(OH)_2 + HSO_3^- = CH_2(OH)SO_3^- + H_2O$ in aqueous solution, J. Phys. Chem., 90, 3213-3217, 10.1021/j100405a033, 1986.

Deister, U., Warneck, P., and Wurzinger, C.: OH Radicals Generated by NO Photolysis in Aqueous Solution: Competition Kinetics and a Study of the Reaction OH + $CH_2(OH)SO_3^-$, Berichte der Bunsengesellschaft für physikalische Chemie, 94, 594-599, 10.1002/bbpc.19900940512, 1990.

Dixon, R. W., and Aasen, H.: Measurement of hydroxymethanesulfonate in atmospheric aerosols, Atmos. Environ., 33, 2023-2029, 10.1016/S1352-2310(98)00416-6, 1999.

Dong, S., and Dasgupta, P. K.: On the formaldehyde-bisulfite-hydroxymethanesulfonate equilibrium, Atmos. Environ., 20, 1635-1637, 10.1016/0004-6981(86)90253-2, 1986.

Dovrou, E., Lim, C. Y., Canagaratna, M. R., Kroll, J. H., Worsnop, D. R., and Keutsch, F. N.: Measurement techniques for identifying and quantifying hydroxymethanesulfonate (HMS) in an aqueous matrix and particulate matter using aerosol mass spectrometry and ion chromatography, Atmos. Meas. Tech., 12, 5303-5315, 10.5194/amt-12-5303-2019, 2019.

Duncan, F., T., Jacob, D. J., and Park, R. J.: The impact of transpacific transport of mineral dust in the United States, Atmos. Environ., 41, 1251-1266, 10.1016/j.atmosenv.2006.09.048, 2007.

Estillore, A. D., Hettiyadura, A. P. S., Qin, Z., Leckrone, E., Wombacher, B., Humphry, T., Stone, E. A., and Grassian, V. H.: Water Uptake and Hygroscopic Growth of Organosulfate Aerosol, Environ. Sci. Technol., 50, 4259-4268, 10.1021/acs.est.5b05014, 2016.

Fahey, K. M., and Pandis, S. N.: Optimizing model performance: variable size resolution in cloud chemistry modeling, Atmos. Environ., 35, 4471-4478, 10.1016/S1352-2310(01)00224-2, 2001.

Fahey, K. M., Carlton, A. G., Pye, H. O. T., Baek, J., Hutzell, W. T., Stanier, C. O., Baker, K. R., Appel, K. W., Jaoui, M., and Offenberg, J. H.: A framework for expanding aqueous chemistry in the Community Multiscale Air Quality (CMAQ) model version 5.1, Geosci. Model Dev., 10, 1587-1605, 10.5194/gmd-10-1587-2017, 2017.

Fairlie, T. D., Jacob, D. J., Dibb, J. E., Alexander, B., Avery, M. A., van Donkelaar, A., and Zhang, L.: Impact of mineral dust on nitrate, sulfate, and ozone in transpacific Asian pollution plumes, Atmos. Chem. Phys., 10, 3999-4012, 10.5194/acp-10-3999-2010, 2010.

Farmer, D. K., Matsunaga, A., Docherty, K. S., Surratt, J. D., Seinfeld, J. H., Ziemann, P. J., and Jimenez, J. L.: Response of an aerosol mass spectrometer to organonitrates and organosulfates and implications for atmospheric chemistry, Proc. Natl. Acad. Sci. U.S.A., 107, 6670-6675, 10.1073/pnas.0912340107, 2010.

Fountoukis, C., and Nenes, A.: ISORROPIA II: a computationally efficient thermodynamic equilibrium model for K^+–Ca^{2+}–Mg^{2+}–NH_4^+–Na^+–SO_4^{2-}–NO_3^-–Cl^-–H_2O aerosols, Atmos. Chem. Phys., 7, 4639-4659, 10.5194/acp-7-4639-2007, 2007.

Froyd, K. D., Murphy, S. M., Murphy, D. M., de Gouw, J. A., Eddingsaas, N. C., and Wennberg, P. O.: Contribution of isoprene-derived organosulfates to free tropospheric aerosol mass, Proc. Natl. Acad. Sci. U.S.A., 107, 21360-21365, 10.1073/pnas.1012561107, 2010.

Ge, C., Wang, J., Carn, S., Yang, K., Ginoux, P., and Krotkov, N.: Satellite-based global volcanic SO_2 emissions and sulfate direct radiative forcing during 2005–2012, J. Geophys. Res. Atmos., 121, 3446-3464, 10.1002/2015jd023134, 2016.

Gelaro, R., McCarty, W., Suárez, M. J., Todling, R., Molod, A., Takacs, L., Randles, C. A., Darmenov, A., Bosilovich, M. G., Reichle, R., Wargan, K., Coy, L., Cullather, R., Draper, C., Akella, S., Buchard, V., Conaty, A., Silva, A. M. d., Gu, W., Kim, G.-K., Koster, R., Lucchesi, R., Merkova, D., Nielsen, J. E., Partyka, G., Pawson, S., Putman, W., Rienecker, M., Schubert, S. D., Sienkiewicz, M., and Zhao, B.: The Modern-Era Retrospective Analysis for Research and Applications, Version 2 (MERRA-2), J. Climate, 30, 5419-5454, 10.1175/jcli-d-16-0758.1, 2017.

Guenther, A. B., Jiang, X., Heald, C. L., Sakulyanontvittaya, T., Duhl, T., Emmons, L. K., and Wang, X.: The Model of Emissions of Gases and Aerosols from Nature version 2.1 (MEGAN2.1): an extended and updated framework for modeling biogenic emissions, Geosci. Model Dev., 5, 1471-1492, 10.5194/gmd-5-1471-2012, 2012.

Hettiyadura, A. P. S., Al-Naiema, I. M., Hughes, D. D., Fang, T., and Stone, E. A.: Organosulfates in Atlanta, Georgia: anthropogenic influences on biogenic secondary organic aerosol formation, Atmos. Chem. Phys., 19, 3191-3206, 10.5194/acp-19-3191-2019, 2019.

Hodshire, A. L., Campuzano-Jost, P., Kodros, J. K., Croft, B., Nault, B. A., Schroder, J. C., Jimenez, J. L., and Pierce, J. R.: The potential role of methanesulfonic acid (MSA) in aerosol formation and growth and the associated radiative forcings, Atmos. Chem. Phys., 19, 3137-3160, 10.5194/acp-19-3137-2019, 2019.

Hoesly, R. M., Smith, S. J., Feng, L., Klimont, Z., Janssens-Maenhout, G., Pitkanen, T., Seibert, J. J., Vu, L., Andres, R. J., Bolt, R. M., Bond, T. C., Dawidowski, L., Kholod, N., Kurokawa, J. I., Li, M., Liu, L., Lu, Z., Moura, M. C. P., O'Rourke, P. R., and Zhang, Q.: Historical (1750–2014) anthropogenic emissions of reactive gases and aerosols from the Community Emissions Data System (CEDS), Geosci. Model Dev., 11, 369-408, 10.5194/gmd-11-369-2018, 2018.

Holmes, C. D., Bertram, T. H., Confer, K. L., Graham, K. A., Ronan, A. C., Wirks, C. K., and Shah, V.: The Role of Clouds in the Tropospheric NOx Cycle: A New Modeling Approach for Cloud Chemistry and Its Global Implications, Geophys. Res. Lett., 46, 4980-4990, 10.1029/2019gl081990, 2019.

Huang, S., Poulain, L., van Pinxteren, D., van Pinxteren, M., Wu, Z., Herrmann, H., and Wiedensohler, A.: Latitudinal and Seasonal Distribution of Particulate MSA over the Atlantic using a Validated Quantification Method with HR-ToF-AMS, Environ. Sci. Technol., 51, 418-426, 10.1021/acs.est.6b03186, 2017.

Hudman, R. C., Moore, N. E., Mebust, A. K., Martin, R. V., Russell, A. R., Valin, L. C., and Cohen, R. C.: Steps towards a mechanistic model of global soil nitric oxide emissions: implementation and space based-constraints, Atmos. Chem. Phys., 12, 7779-7795, 10.5194/acp-12-7779-2012, 2012.

Jacob, D. J.: Chemistry of OH in remote clouds and its role in the production of formic acid and peroxymonosulfate, J. Geophys. Res. Atmos., 91, 9807-9826, 10.1029/JD091iD09p09807, 1986.

Jacob, D. J., Gottlieb, E. W., and Prather, M. J.: Chemistry of a polluted cloudy boundary layer, J. Geophys. Res. Atmos., 94, 12975-13002, 10.1029/JD094iD10p12975, 1989.

Jacob, D. J.: Heterogeneous chemistry and tropospheric ozone, Atmos. Environ., 34, 2131-2159, 10.1016/S1352-2310(99)00462-8, 2000.

Jaeglé, L., Quinn, P. K., Bates, T. S., Alexander, B., and Lin, J. T.: Global distribution of sea salt aerosols: new constraints from in situ and remote sensing observations, Atmos. Chem. Phys., 11, 3137-3157, 10.5194/acp-11-3137-2011, 2011.

Jaeglé, L., Shah, V., Thornton, J. A., Lopez-Hilfiker, F. D., Lee, B. H., McDuffie, E. E., Fibiger, D., Brown, S. S., Veres, P., Sparks, T. L., Ebben, C. J., Wooldridge, P. J., Kenagy, H. S., Cohen, R. C., Weinheimer, A. J., Campos, T. L., Montzka, D. D., Digangi, J. P., Wolfe, G. M., Hanisco, T., Schroder, J. C., Campuzano-Jost, P., Day, D. A., Jimenez, J. L., Sullivan, A. P., Guo, H., and Weber, R. J.: Nitrogen Oxides Emissions, Chemistry, Deposition, and Export Over the Northeast United States During the WINTER Aircraft Campaign, J. Geophys. Res. Atmos., 123, 12,368-312,393, 10.1029/2018jd029133, 2018.

Keller, C. A., Long, M. S., Yantosca, R. M., Da Silva, A. M., Pawson, S., and Jacob, D. J.: HEMCO v1.0: a versatile, ESMF-compliant component for calculating emissions in atmospheric models, Geosci. Model Dev., 7, 1409-1417, 10.5194/gmd-7-1409-2014, 2014.

Kennedy, A. D., Dong, X., Xi, B., Xie, S., Zhang, Y., and Chen, J.: A Comparison of MERRA and NARR Reanalyses with the DOE ARM SGP Data, J. Climate, 24, 4541-4557, 10.1175/2011jcli3978.1, 2011.

Kok, G. L., Gitlin, S. N., and Lazrus, A. L.: Kinetics of the formation and decomposition of hydroxymethanesulfonate, J. Geophys. Res. Atmos., 91, 2801-2804, 10.1029/JD091iD02p02801, 1986.

Kong, L., Tang, X., Zhu, J., Wang, Z., Pan, Y., Wu, H., Wu, L., Wu, Q., He, Y., Tian, S., Xie, Y., Liu, Z., Sui, W., Han, L., and Carmichael, G.: Improved Inversion of Monthly Ammonia Emissions in China Based on the Chinese Ammonia Monitoring Network and Ensemble Kalman Filter, Environ. Sci. Technol., 53, 12529-12538, 10.1021/acs.est.9b02701, 2019.

Lagrange, J., Wenger, G., and Lagrange, P.: Kinetic study of HMSA formation and decomposition: Tropospheric relevance, J. Chim. Phys., 96, 610-633, 1999.

Lana, A., Bell, T. G., Simó, R., Vallina, S. M., Ballabrera-Poy, J., Kettle, A. J., Dachs, J., Bopp, L., Saltzman, E. S., Stefels, J., Johnson, J. E., and Liss, P. S.: An updated climatology of surface dimethlysulfide concentrations and emission fluxes in the global ocean, Global Biogeochem. Cycles, 25, 10.1029/2010gb003850, 2011.

Li, J., Zhang, Y.-L., Cao, F., Zhang, W., Fan, M., Lee, X., and Michalski, G.: Stable Sulfur Isotopes Revealed a Major Role of Transition-Metal Ion-Catalyzed SO2 Oxidation in Haze Episodes, Environ. Sci. Technol., 54, 2626-2634, 10.1021/acs.est.9b07150, 2020.

Li, M., Zhang, Q., Kurokawa, J. I., Woo, J. H., He, K., Lu, Z., Ohara, T., Song, Y., Streets, D. G., Carmichael, G. R., Cheng, Y., Hong, C., Huo, H., Jiang, X., Kang, S., Liu, F., Su, H., and Zheng, B.: MIX: a mosaic Asian anthropogenic emission inventory under the international collaboration framework of the MICS-Asia and HTAP, Atmos. Chem. Phys., 17, 935-963, 10.5194/acp-17-935-2017, 2017.

Liu, M., Huang, X., Song, Y., Tang, J., Cao, J., Zhang, X., Zhang, Q., Wang, S., Xu, T., Kang, L., Cai, X., Zhang, H., Yang, F., Wang, H., Yu, J. Z., Lau, A. K. H., He, L., Huang, X., Duan, L., Ding, A., Xue, L., Gao, J., Liu, B., and Zhu, T.: Ammonia emission control in China would mitigate haze pollution and nitrogen deposition, but worsen acid rain, Proc. Natl. Acad. Sci. U.S.A., 116, 7760-7765, 10.1073/pnas.1814880116, 2019.

Liu, Q.: Kinetics of aqueous phase reactions related to ozone depletion in the Arctic troposphere: Bromine chloride hydrolysis, bromide ion with ozone, and sulfur (IV) with bromine and hypobromous acid, Purdue University, 2002.

Liu, T., and Abbatt, J. P. D.: An Experimental Assessment of the Importance of S(IV) Oxidation by Hypohalous Acids in the Marine Atmosphere, Geophys. Res. Lett., 47, e2019GL086465, 10.1029/2019gl086465, 2020.

Liu, T., Clegg, S. L., and Abbatt, J. P. D.: Fast oxidation of sulfur dioxide by hydrogen peroxide in deliquesced aerosol particles, Proc. Natl. Acad. Sci. U.S.A., 117, 1354-1359, 10.1073/pnas.1916401117, 2020.

Luo, G., Yu, F., and Schwab, J.: Revised treatment of wet scavenging processes dramatically improves GEOS-Chem 12.0.0 simulations of surface nitric acid, nitrate, and ammonium over the United States, Geosci. Model Dev., 12, 3439-3447, 10.5194/gmd-12-3439-2019, 2019.

Luo, G., Yu, F., and Moch, J. M.: Further improvement of wet process treatments in GEOS-Chem v12.6.0: Impact on global distributions of aerosol precursors and aerosols, Geosci. Model Dev. Discuss., 2020, 1-39, 10.5194/gmd-2020-11, 2020.

Ma, T., Furutani, H., Duan, F., Kimoto, T., Jiang, J., Zhang, Q., Xu, X., Wang, Y., Gao, J., Geng, G., Li, M., Song, S., Ma, Y., Che, F., Wang, J., Zhu, L., Huang, T., Toyoda, M., and He, K.: Contribution of hydroxymethanesulfonate (HMS) to severe winter haze in the North China Plain, Atmos. Chem. Phys., 20, 5887-5897, 10.5194/acp-20-5887-2020, 2020.

Marais, E. A., and Wiedinmyer, C.: Air Quality Impact of Diffuse and Inefficient Combustion Emissions in Africa (DICE-Africa), Environ. Sci. Technol., 50, 10739-10745, 10.1021/acs.est.6b02602, 2016.

Martin, L. R., Damschen, D. E., and Judeikis, H. S.: The reactions of nitrogen oxides with SO_2 in aqueous aerosols, Atmos. Environ., 15, 191-195, 10.1016/0004-6981(81)90010-X, 1981.

Martin, L. R., Easton, M. P., Foster, J. W., and Hill, M. W.: Oxidation of hydroxymethanesulfonic acid by Fenton's reagent, Atmos. Environ., 23, 563-568, 10.1016/0004-6981(89)90005-X, 1989.

Miao, H., Wang, X., Liu, Y., and Wu, G.: An evaluation of cloud vertical structure in three reanalyses against CloudSat/cloud-aerosol lidar and infrared pathfinder satellite observations, Atmos. Sci. Lett., 20, e906, 10.1002/asl.906, 2019.

Moch, J. M., Dovrou, E., Mickley, L. J., Keutsch, F. N., Cheng, Y., Jacob, D. J., Jiang, J., Li, M., Munger, J. W., Qiao, X., and Zhang, Q.: Contribution of Hydroxymethane Sulfonate to Ambient Particulate Matter: A Potential Explanation for High Particulate Sulfur During Severe Winter Haze in Beijing, Geophys. Res. Lett., 45, 11969-11979, 10.1029/2018GL079309, 2018.

Molod, A.: Constraints on the Profiles of Total Water PDF in AGCMs from AIRS and a High-Resolution Model, J. Climate, 25, 8341-8352, 10.1175/jcli-d-11-00412.1, 2012.

Molod, A., Takacs, L., Suarez, M., and Bacmeister, J.: Development of the GEOS-5 atmospheric general circulation model: evolution from MERRA to MERRA2, Geosci. Model Dev., 8, 1339-1356, 10.5194/gmd-8-1339-2015, 2015.

Müller, B., and Heal, M. R.: The mass accommodation coefficient of ozone on an aqueous surface, Phys. Chem. Chem. Phys., 4, 3365-3369, 10.1039/B202491H, 2002.

Munger, J. W., Jacob, D. J., and Hoffmann, M. R.: The occurrence of bisulfite-aldehyde addition products in fog- and cloudwater, J. Atmos. Chem., 1, 335-350, 10.1007/BF00053799, 1984.

Munger, J. W., Tiller, C., and Hoffmann, M. R.: Identification of hydroxymethanesulfonate in fog water, Science, 231, 247-249, 10.1126/science.231.4735.247, 1986.

Murray, L. T., Jacob, D. J., Logan, J. A., Hudman, R. C., and Koshak, W. J.: Optimized regional and interannual variability of lightning in a global chemical transport model constrained by LIS/OTD satellite data, J. Geophys. Res. Atmos., 117, 10.1029/2012jd017934, 2012.

Nickovic, S., Vukovic, A., Vujadinovic, M., Djurdjevic, V., and Pejanovic, G.: Technical Note: High-resolution mineralogical database of dust-productive soils for atmospheric dust modeling, Atmos. Chem. Phys., 12, 845-855, 10.5194/acp-12-845-2012, 2012.

Olson, T. M., and Hoffmann, M. R.: Hydroxyalkylsulfonate formation: Its role as a S(IV) reservoir in atmospheric water droplets, Atmos. Environ., 23, 985-997, 10.1016/0004-6981(89)90302-8, 1989.

Olson, T. M., and Fessenden, R. W.: Pulse radiolysis study of the reaction of hydroxyl radicals with methanesulfonate and hydroxymethanesulfonate, J. Phys. Chem., 96, 3317-3320, 10.1021/j100187a027, 1992.

Pan, Y., Tian, S., Liu, D., Fang, Y., Zhu, X., Gao, M., Gao, J., Michalski, G., and Wang, Y.: Isotopic evidence for enhanced fossil fuel sources of aerosol ammonium in the urban atmosphere, Environ. Pollut., 238, 942-947, 10.1016/j.envpol.2018.03.038, 2018.

Pandis, S. N., and Seinfeld, J. H.: Sensitivity analysis of a chemical mechanism for aqueous‐phase atmospheric chemistry, J. Geophys. Res. Atmos., 94, 1105-1126, 10.1029/JD094iD01p01105, 1989.

Park, R. J., Jacob, D. J., Field, B. D., Yantosca, R. M., and Chin, M.: Natural and transboundary pollution influences on sulfate-nitrate-ammonium aerosols in the United States: Implications for policy, J. Geophys. Res. Atmos., 109, 10.1029/2003jd004473, 2004.

Philip, S., Martin, R. V., and Keller, C. A.: Sensitivity of chemistry-transport model simulations to the duration of chemical and transport operators: a case study with GEOS-Chem v10-01, Geosci. Model Dev., 9, 1683-1695, 10.5194/gmd-9-1683-2016, 2016.

Philip, S., Martin, R. V., Snider, G., Weagle, C. L., van Donkelaar, A., Brauer, M., Henze, D. K., Klimont, Z., Venkataraman, C., Guttikunda, S. K., and Zhang, Q.: Anthropogenic fugitive, combustion and industrial dust is a significant, underrepresented fine particulate matter source in global atmospheric models, Environ. Res. Lett., 12, 044018, 10.1088/1748-9326/aa65a4, 2017.

Phinney, L., Richard Leaitch, W., Lohmann, U., Boudries, H., Worsnop, D. R., Jayne, J. T., Toom-Sauntry, D., Wadleigh, M., Sharma, S., and Shantz, N.: Characterization of the aerosol over the sub-arctic north east Pacific Ocean, Deep Sea Res. Part II Top. Stud. Oceanogr., 53, 2410-2433, 10.1016/j.dsr2.2006.05.044, 2006.

Ravishankara, A. R.: Heterogeneous and Multiphase Chemistry in the Troposphere, Science, 276, 1058-1065, 10.1126/science.276.5315.1058, 1997.

Richards, L. W., Anderson, J. A., Blumenthal, D. L., McDonald, J. A., Kok, G. L., and Lazrus, A. L.: Hydrogen peroxide and sulfur (IV) in Los Angeles cloud water, Atmos. Environ., 17, 911-914, 10.1016/0004-6981(83)90458-4, 1983.

Riva, M., Chen, Y., Zhang, Y., Lei, Z., Olson, N. E., Boyer, H. C., Narayan, S., Yee, L. D., Green, H. S., Cui, T., Zhang, Z., Baumann, K., Fort, M., Edgerton, E., Budisulistiorini, S. H., Rose, C. A., Ribeiro, I. O., e Oliveira, R. L., dos Santos, E. O., Machado, C. M. D., Szopa, S., Zhao, Y., Alves, E. G., de Sá, S. S., Hu, W., Knipping, E. M., Shaw, S. L., Duvoisin Junior, S., de Souza, R. A. F., Palm, B. B., Jimenez, J.-L., Glasius, M., Goldstein, A. H., Pye, H. O. T., Gold, A., Turpin, B. J., Vizuete, W., Martin, S. T., Thornton, J. A., Dutcher, C. S., Ault, A. P., and Surratt, J. D.: Increasing Isoprene Epoxydiol-to-Inorganic Sulfate Aerosol Ratio Results in Extensive Conversion of Inorganic Sulfate to Organosulfur Forms: Implications for Aerosol Physicochemical Properties, Environ. Sci. Technol., 53, 8682-8694, 10.1021/acs.est.9b01019, 2019.

Sander, R.: Compilation of Henry's law constants (version 4.0) for water as solvent, Atmos. Chem. Phys., 15, 4399-4981, 10.5194/acp-15-4399-2015, 2015.

Scheinhardt, S., van Pinxteren, D., Müller, K., Spindler, G., and Herrmann, H.: Hydroxymethanesulfonic acid in size-segregated aerosol particles at nine sites in Germany, Atmos. Chem. Phys., 14, 4531-4538, 10.5194/acp-14-4531-2014, 2014.

Schwartz, S. E., and Freiberg, J. E.: Mass-transport limitation to the rate of reaction of gases in liquid droplets: Application to oxidation of SO_2 in aqueous solutions, Atmos. Environ., 15, 1129-1144, 10.1016/0004-6981(81)90303-6, 1981.

Sciare, J., Favez, O., Sarda-Estève, R., Oikonomou, K., Cachier, H., and Kazan, V.: Long-term observations of carbonaceous aerosols in the Austral Ocean atmosphere: Evidence of a biogenic marine organic source, J. Geophys. Res. Atmos., 114, 10.1029/2009jd011998, 2009.

Seinfeld, J. H., and Pandis, S. N.: Atmospheric chemistry and physics: from air pollution to climate change, Third ed., John Wiley & Sons, Inc., Hoboken, New Jersey, 2016.

Shah, V., Jaeglé, L., Thornton, J. A., Lopez-Hilfiker, F. D., Lee, B. H., Schroder, J. C., Campuzano-Jost, P., Jimenez, J. L., Guo, H., Sullivan, A. P., Weber, R. J., Green, J. R., Fiddler, M. N., Bililign, S., Campos, T. L., Stell, M., Weinheimer, A. J., Montzka, D. D., and Brown, S. S.: Chemical feedbacks weaken the wintertime response of particulate sulfate and nitrate to emissions reductions over the eastern United States, Proc. Natl. Acad. Sci. U.S.A., 115, 8110-8115, 10.1073/pnas.1803295115, 2018.

Shao, J., Chen, Q., Wang, Y., Lu, X., He, P., Sun, Y., Shah, V., Martin, R. V., Philip, S., Song, S., Zhao, Y., Xie, Z., Zhang, L., and Alexander, B.: Heterogeneous sulfate aerosol formation mechanisms during wintertime Chinese haze events: air quality model assessment using observations of sulfate oxygen isotopes in Beijing, Atmos. Chem. Phys., 19, 6107-6123, 10.5194/acp-19-6107-2019, 2019.

Simone, N. W., Stettler, M. E. J., and Barrett, S. R. H.: Rapid estimation of global civil aviation emissions with uncertainty quantification, Transp. Res. D Transp. Environ., 25, 33-41, 10.1016/j.trd.2013.07.001, 2013.

Sitnov, S. A., Mokhov, I. I., and Gorchakov, G. I.: The link between smoke blanketing of European Russia in summer 2016, Siberian wildfires and anomalies of large-scale atmospheric circulation, Doklady Earth Sciences, 472, 190-195, 10.1134/S1028334X17020052, 2017.

Song, S., Gao, M., Xu, W., Shao, J., Shi, G., Wang, S., Wang, Y., Sun, Y., and McElroy, M. B.: Fine-particle pH for Beijing winter haze as inferred from different thermodynamic equilibrium models, Atmos. Chem. Phys., 18, 7423-7438, 10.5194/acp-18-7423-2018, 2018.

Song, S., Gao, M., Xu, W., Sun, Y., Worsnop, D. R., Jayne, J. T., Zhang, Y., Zhu, L., Li, M., Zhou, Z., Cheng, C., Lv, Y., Wang, Y., Peng, W., Xu, X., Lin, N., Wang, Y., Wang, S., Munger, J. W., Jacob, D. J., and McElroy, M. B.: Possible heterogeneous chemistry of hydroxymethanesulfonate (HMS) in northern China winter haze, Atmos. Chem. Phys., 19, 1357-1371, 10.5194/acp-19-1357-2019, 2019a.

Song, S., Nenes, A., Gao, M., Zhang, Y., Liu, P., Shao, J., Ye, D., Xu, W., Lei, L., Sun, Y., Liu, B., Wang, S., and McElroy, M. B.: Thermodynamic Modeling Suggests Declines in Water Uptake and Acidity of Inorganic Aerosols in Beijing Winter Haze Events during 2014/2015–2018/2019, Environ. Sci. Technol. Lett., 6, 752-760, 10.1021/acs.estlett.9b00621, 2019b.

Sørensen, P. E., and Andersen, V. S.: The formaldehyde-hydrogen sulphite system in alkaline aqueous solution. Kinetics, mechanisms, and equilibria, Acta Chemica Scandinavica, 24, 1301-1306, 10.3891/acta.chem.scand.24-1301, 1970.

Sorooshian, A., Crosbie, E., Maudlin, L. C., Youn, J. S., Wang, Z., Shingler, T., Ortega, A. M., Hersey, S., and Woods, R. K.: Surface and airborne measurements of organosulfur and methanesulfonate over the western United States and coastal areas, J. Geophys. Res. Atmos., 120, 8535-8548, 10.1002/2015JD023822, 2015.

Stengel, M., Schlundt, C., Stapelberg, S., Sus, O., Eliasson, S., Willén, U., and Meirink, J. F.: Comparing ERA-Interim clouds with satellite observations using a simplified satellite simulator, Atmos. Chem. Phys., 18, 17601-17614, 10.5194/acp-18-17601-2018, 2018.

Surratt, J. D., Kroll, J. H., Kleindienst, T. E., Edney, E. O., Claeys, M., Sorooshian, A., Ng, N. L., Offenberg, J. H., Lewandowski, M., Jaoui, M., Flagan, R. C., and Seinfeld, J. H.: Evidence for Organosulfates in Secondary Organic Aerosol, Environ. Sci. Technol., 41, 517-527, 10.1021/es062081q, 2007.

Surratt, J. D., Chan, A. W. H., Eddingsaas, N. C., Chan, M., Loza, C. L., Kwan, A. J., Hersey, S. P., Flagan, R. C., Wennberg, P. O., and Seinfeld, J. H.: Reactive intermediates revealed in secondary organic aerosol formation from isoprene, Proc. Natl. Acad. Sci. U.S.A., 107, 6640-6645, 10.1073/pnas.0911114107, 2010.

Suzuki, Y., Kawakami, M., and Akasaka, K.: 1H NMR Application for Characterizing Water-Soluble Organic Compounds in Urban Atmospheric Particles, Environ. Sci. Technol., 35, 2656-2664, 10.1021/es001861a, 2001.

Tilgner, A., and Herrmann, H.: Tropospheric Aqueous-Phase OH Oxidation Chemistry: Current Understanding, Uptake of Highly Oxidized Organics and Its Effects, in: Multiphase Environmental Chemistry in the Atmosphere, ACS Symposium Series, 1299, American Chemical Society, 49-85, 2018.

Travis, K. R., Jacob, D. J., Fisher, J. A., Kim, P. S., Marais, E. A., Zhu, L., Yu, K., Miller, C. C., Yantosca, R. M., Sulprizio, M. P., Thompson, A. M., Wennberg, P. O., Crounse, J. D., St. Clair, J. M., Cohen, R. C., Laughner, J. L., Dibb, J. E., Hall, S. R., Ullmann, K., Wolfe, G. M., Pollack, I. B., Peischl, J., Neuman, J. A., and Zhou, X.: Why do models overestimate surface ozone in the Southeast United States?, Atmos. Chem. Phys., 16, 13561-13577, 10.5194/acp-16-13561-2016, 2016.

Troy, R. C., and Margerum, D. W.: Non-metal redox kinetics: hypobromite and hypobromous acid reactions with iodide and with sulfite and the hydrolysis of bromosulfate, Inorg. Chem., 30, 3538-3543, 10.1021/ic00018a028, 1991.

van der Werf, G. R., Randerson, J. T., Giglio, L., van Leeuwen, T. T., Chen, Y., Rogers, B. M., Mu, M., van Marle, M. J. E., Morton, D. C., Collatz, G. J., Yokelson, R. J., and Kasibhatla, P. S.: Global fire emissions estimates during 1997–2016, Earth Syst. Sci. Data, 9, 697-720, 10.5194/essd-9-697-2017, 2017.

Wang, G., Zhang, R., Gomez, M. E., Yang, L., Levy Zamora, M., Hu, M., Lin, Y., Peng, J., Guo, S., Meng, J., Li, J., Cheng, C., Hu, T., Ren, Y., Wang, Y., Gao, J., Cao, J., An, Z., Zhou, W., Li, G., Wang, J., Tian, P., Marrero-Ortiz, W., Secrest, J., Du, Z., Zheng, J., Shang, D., Zeng, L., Shao, M., Wang, W., Huang, Y., Wang, Y., Zhu, Y., Li, Y., Hu, J., Pan, B., Cai, L., Cheng, Y., Ji, Y., Zhang, F., Rosenfeld, D., Liss, P. S., Duce, R. A., Kolb, C. E., and Molina, M. J.: Persistent sulfate formation from London Fog to Chinese haze, Proc. Natl. Acad. Sci. U.S.A., 113, 13630-13635, 10.1073/pnas.1616540113, 2016.

Whiteaker, J. R., and Prather, K. A.: Hydroxymethanesulfonate as a tracer for fog processing of individual aerosol particles, Atmos. Environ., 37, 1033-1043, 10.1016/S1352-2310(02)01029-4, 2003.

Winkelman, J. G. M., Voorwinde, O. K., Ottens, M., Beenackers, A. A. C. M., and Janssen, L. P. B. M.: Kinetics and chemical equilibrium of the hydration of formaldehyde, Chem. Eng. Sci., 57, 4067-4076, 10.1016/S0009-2509(02)00358-5, 2002.

Xu, L., Guo, H., Boyd, C. M., Klein, M., Bougiatioti, A., Cerully, K. M., Hite, J. R., Isaacman-VanWertz, G., Kreisberg, N. M., Knote, C., Olson, K., Koss, A., Goldstein, A. H., Hering, S. V., de Gouw, J., Baumann, K., Lee, S.-H., Nenes, A., Weber, R. J., and Ng, N. L.: Effects of anthropogenic emissions on aerosol formation from isoprene and monoterpenes in the southeastern United States, Proc. Natl. Acad. Sci. U.S.A., 112, 37-42, 10.1073/pnas.1417609112, 2015.

Xu, W., Ovadnevaite, J., Fossum, K. N., Lin, C., Huang, R. J., O'Dowd, C., and Ceburnis, D.: Aerosol hygroscopicity and its link to chemical composition in the coastal atmosphere of Mace Head: marine and continental air masses, Atmos. Chem. Phys., 20, 3777-3791, 10.5194/acp-20-3777-2020, 2020.

Yuen, P.-F., Hegg, D. A., Larson, T. V., and Barth, M. C.: Parameterization of Heterogeneous Droplet Chemistry for Use in Bulk Cloud Models, J. Appl. Meteorol., 35, 679-689, 10.1175/1520-0450(1996)035<0679:Pohdcf>2.0.Co;2, 1996.

Zhang, D., Lv, G., Sun, X., Zhang, C., and Li, Z.: A theoretical study on the formation and oxidation mechanism of hydroxyalkylsulfonate in the atmospheric aqueous phase, RSC Adv., 9, 27334-27340, 10.1039/C9RA05193G, 2019.

Zheng, B., Zhang, Q., Zhang, Y., He, K. B., Wang, K., Zheng, G. J., Duan, F. K., Ma, Y. L., and Kimoto, T.: Heterogeneous chemistry: a mechanism missing in current models to explain secondary inorganic aerosol formation during the January 2013 haze episode in North China, Atmos. Chem. Phys., 15, 2031-2049, 10.5194/acp-15-2031-2015, 2015.

Zheng, B., Tong, D., Li, M., Liu, F., Hong, C., Geng, G., Li, H., Li, X., Peng, L., Qi, J., Yan, L., Zhang, Y., Zhao, H., Zheng, Y., He, K., and Zhang, Q.: Trends in China's anthropogenic emissions since 2010 as the consequence of clean air actions, Atmos. Chem. Phys., 18, 14095-14111, 10.5194/acp-18-14095-2018, 2018.

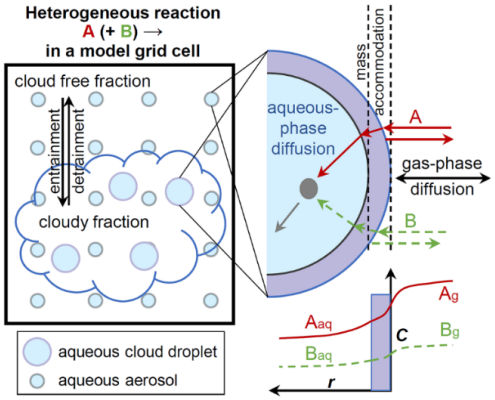

Figure 1. Schematic of physicochemical processes that control the heterogeneous reaction of a molecule A (with another molecule B) in a model grid cell. (**Left**). Entrainment and detrainment of air into and out from clouds. The volume occupied by aqueous clouds in the grid cell is represented by the cloud fraction (f_c), which is provided by the MERRA-2 meteorological reanalysis in this study. The cloud free fraction is thus $1-f_c$. Aqueous aerosols are assumed to be evenly distributed in the grid cell. For aqueous cloud droplets and aqueous aerosols, the same mass transport processes are considered and are shown in the right panel. (**Top Right**). Gas-phase, interfacial, and aqueous-phase mass transport limitations for the molecules A and B. (**Bottom Right**). Concentration (C) profiles of A and B are a function of radial distance (r) from the surface of a spherical particle. The subscripts g and aq refer to gas and aqueous phases, respectively. The concentrations are in arbitrary units and their scales are different for gas and aqueous phases. The entrainment/detrainment processes for clouds have been described in detail by Holmes et al. (2019). The right panel is adapted from Figure 4 in Ravishankara (1997).

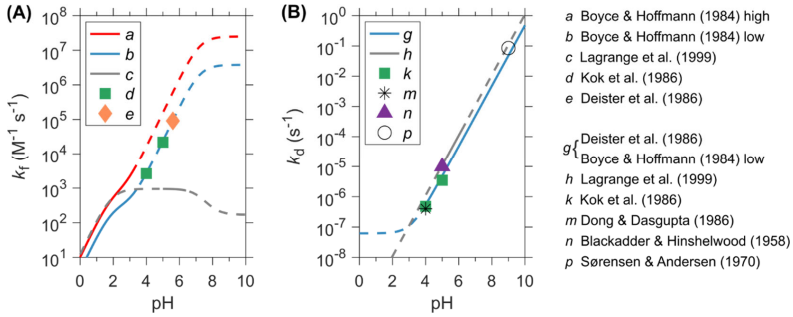

Figure 2. Comparison of rate constants for the formation (panel **A**, k_f in M^{-1} s^{-1}) and decomposition (panel **B**, k_d in s^{-1}) of HMS from the available laboratory studies. Data are shown as a function of pH. Unless otherwise noted, rate constants are determined at or corrected to 25 °C and dilute condition ($\mu < 0.01$ M). For *a*, *b*, *c*, *g*, and *h*, the solid curves show the range of pH where these experiments are performed, whereas the dash curves indicate the extrapolated values. Other experiments (*d*, *e*, *k*, *m*, *n*, and *p*) are performed at discrete pH and shown by symbols. (*a*) the high k_f is from Boyce and Hoffmann (1984) at $\mu = 1$ M. (*b*) the low k_f is also from Boyce and Hoffmann (1984) and corrected for μ and K_h. (*c*) Lagrange et al. (1999): $k_f = K_h \times \left(0.73 \times x_{HSO_3^-} + 0.13 \times x_{SO_3^{2-}}\right)$ M^{-1} s^{-1}. (*d*) Kok et al. (1986): the reported k_f is limited by the dehydration rate of $CH_2(OH)_2$, k_{dh}, and is thus corrected here. (*e*) is calculated using the k_d and K_{eq} determined by Deister et al. (1986) and is also corrected for k_{dh}. The calculated k_f values are 2.6×10^3, 2.2×10^4, and 9.1×10^4 $M^{-1}s^{-1}$, respectively, at pH = 4, 5, and 5.6 in (*d*) and (*e*). For comparison, the extrapolation of the low k_f data (*b*) are 2.7×10^3, 2.4×10^4, and 9.3×10^4 $M^{-1}s^{-1}$, respectively, at pH = 4, 5, and 5.6. (*g*) k_d is calculated using the K_{eq} from Deister et al. (1986) and the low k_f from Boyce and Hoffmann (1984). (*h*) Lagrange et al. (1999): $k_d = 1.1 \times 10^4 \times \left(K_w/[H^+]\right)$ at $\mu = 1$ M in the presence of H_2O_2. (*k*) Kok et al. (1986) measured k_d of 4.8×10^{-7} and 3.5×10^{-6} s^{-1}, respectively, at pH 4 and 5. (*m*) Dong and Dasgupta (1986) measured K_{eq} at pH 4 and $\mu = 0.05$ M, which translated to a k_d of 4×10^{-7} s^{-1}. (*n*) Blackadder and Hinshelwood (1958): $k_d = 1 \times 10^{-5}$ s^{-1} at pH 5 and $\mu \approx 0.1$ M. (*p*) Sørensen and Andersen (1970): $k_d = 8.5 \times 10^{-2}$ s^{-1} at pH 9 and $\mu = 0.1$ M. For comparison, values of k_d calculated by (*g*) are 5.4×10^{-7}, 4.9×10^{-6}, and 4.8×10^{-2} s^{-1} at pH 4, 5, and 9, respectively.

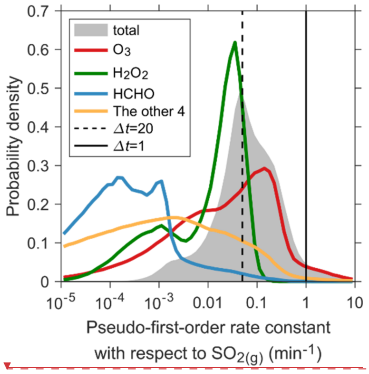

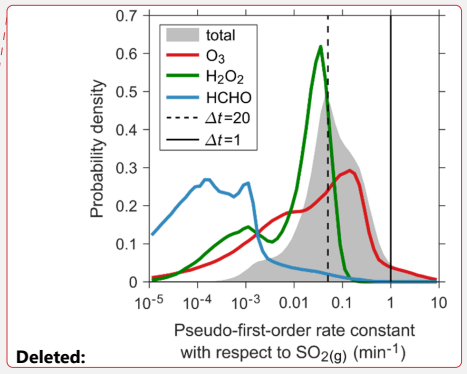

Deleted:

Figure 3. Probability density distributions of the pseudo-first-order rate constants with respect to $SO_{2(g)}$ for cloud reactions in the control simulation. The shaded area shows the sum of rate constants for the 7 reactions consuming SO_2. The red, green, blue, and orange curves indicate the distributions for reactions with O_3, H_2O_2, HCHO, and the sum of rate constants for the other 4 reactions consuming SO_2 (TMI+O_2, NO_2, HONO, and HOBr), respectively. Data shown are for the first week of July and in the lower troposphere (13 vertical layers above surface up to about 800 hPa). Since the chemistry time step (Δt) of this simulation is 20 min, there are 504 steps in this week. The total number of data points is 72 × 46 (number of 5° × 4° grids) × 13 (vertical layers) × 504 ≈ 2.2×10^7. About 1.4×10^7 data points have aqueous clouds (cloud fraction $f_c > 0$), accounting for about 2/3. The probability density distributions are plotted based on these data points. The dashed and solid vertical black lines indicate the rate constants corresponding to Δt of 20 min and 1 min, respectively.

Deleted: and

Deleted: and

Formatted: Subscript

Formatted: Subscript

Formatted: Subscript

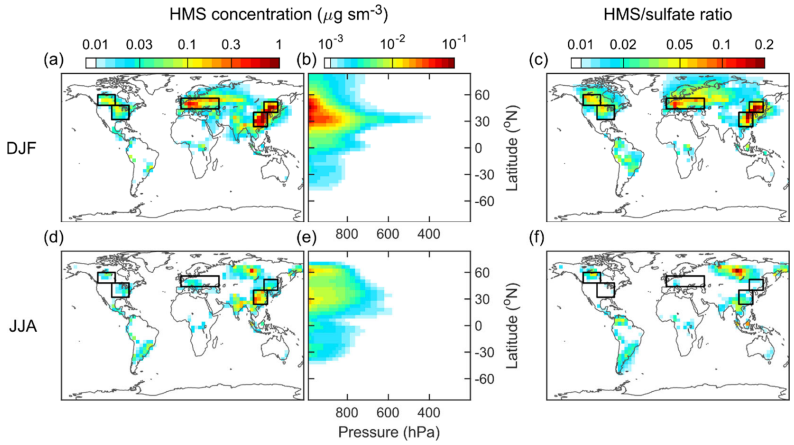

Figure 4. Distributions of HMS concentrations and the molar ratios of HMS to sulfate modeled by the default simulation. Top and bottom panels show results for DJF (December–January–February) and JJA (June–July–August), respectively. (a), (c), (d), and (f) are the horizontal distributions in the surface layer. (b) and (e) are the vertical distributions of the zonal averages from surface to 200 hPa. The concentration unit is μg sm^{-3}, where 1 sm^3 equals 1 m^3 at 273.15 K and 1013.25 hPa. The color bars are not linear and differ in the three columns. The

same color bars are used for each pair of the top and bottom panels. The black-outline boxes indicate the three regions selected for quantitative analysis.

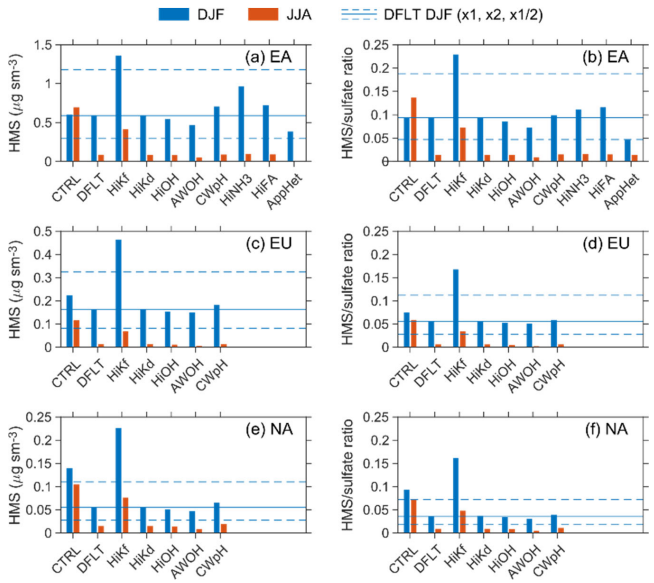

Figure 5. Comparison of the modeled surface HMS concentrations (left) and HMS/sulfate molar ratios (right) from different simulations for three regions and two seasons. EA, EU, and NA are East Asia, Europe, and North America, respectively. DJF and JJA represent December–January–February and June–July–August, respectively. The solid and dashed lines indicate the DJF value from the default (DFLT) simulation and its double and half. The vertical axis differs in the left panels.

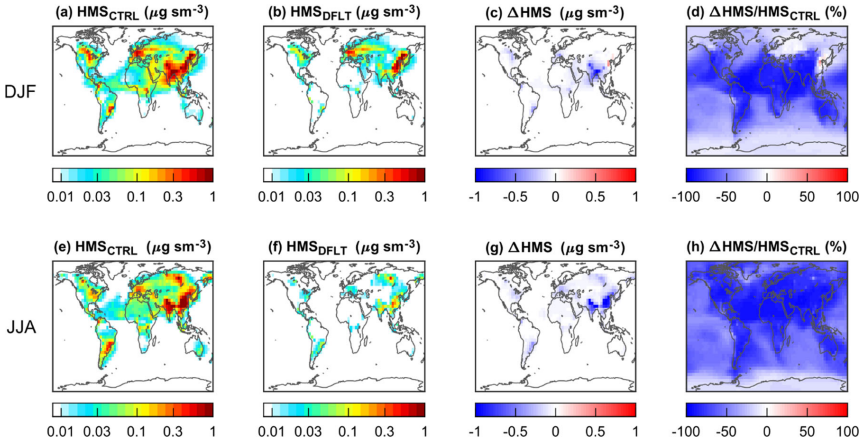

Figure 6. Surface concentrations of HMS from the control (CTRL) and default (DFLT) simulations in two seasons. Top and bottom panels show results for DJF (December–January–February) and JJA (June–July–August), respectively. (c) is the absolute difference between these two simulations: b−a. (d) is their relative difference: (b/a−1)×100%. Similarly, (g) is the absolute difference between (e) and (f): f−e, and (h) the relative difference between them: (*f*/e−1)×100%. The color bars in (a), (b), (e), and (f) are not linear.

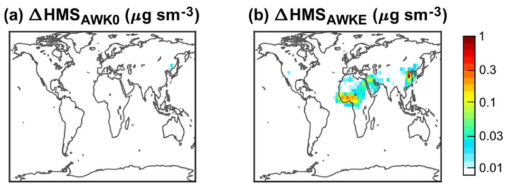

Figure 7. Difference in surface HMS concentrations in DJF (December–January–February) between two sensitivity simulations (AWK0 (a) and AWKE (b)) and the default simulation (DFLT). The color bar is not linear.

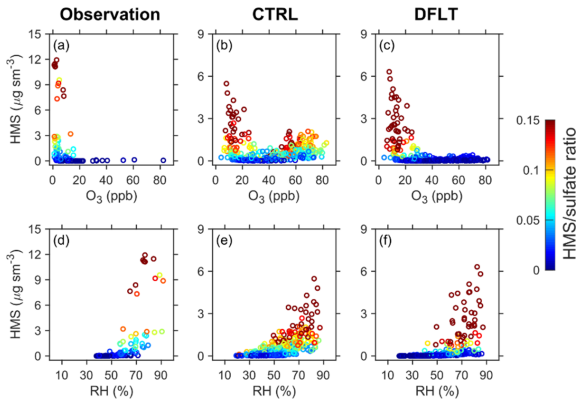

Figure 8. Relationship between HMS concentrations and O_3 mixing ratios (top) and RH (bottom) in northern China. Data from observations, the control (CTRL), and the default (DFLT) simulations are presented in (a) and (d), (b) and (e), and (c) and (f), respectively. HMS/sulfate molar ratios are indicated by the color scale. The observational data in (a) and (d) were collected in Beijing by Ma et al. (2020). There were 69 daily (and 8 half-day) samples in the 2015/16 and 2016/17 winter seasons. The model data are obtained from the grid cell covering Beijing with 366 daily samples. The vertical axes differ in the panels of observations and model simulations.

Table 1. Aqueous-phase reaction rate expressions.

Reaction	Rate expression ($M\ s^{-1}$)	Reference and note
$SO_2 + HCHO \rightarrow HMS$	$R_{aq} = k_f[HCHO]_{aq}[SO_2^T]_{aq} = \left(k_1 x_{HSO_3^-} + k_2 x_{SO_3^{2-}}\right)[HCHO]_{aq}[SO_2^T]_{aq}$ $k_{1,high} = 7.9 \times 10^2 \times \exp\left(-3000 \times (1/T - 1/298)\right)\ M^{-1}\ s^{-1}$ $k_{2,high} = 2.5 \times 10^7 \times \exp\left(-2500 \times (1/T - 1/298)\right)\ M^{-1}\ s^{-1}$ $k_{1,low} = 3.2 \times 10^2 \times \exp\left(-2700 \times (1/T - 1/298)\right)\ M^{-1}\ s^{-1}$ $k_{2,low} = 3.8 \times 10^6 \times \exp\left(-2500 \times (1/T - 1/298)\right)\ M^{-1}\ s^{-1}$	Boyce and Hoffmann (1984)
$HMS \rightarrow SO_2 + HCHO$	$k_d = 6.2 \times 10^{-8} \times \exp\left(-11400 \times (1/T - 1/298)\right)$ $+4.8 \times 10^3 \times (K_w/[H^+]) \times \exp\left(-4700 \times (1/T - 1/298)\right)\ s^{-1}$	Boyce and Hoffmann (1984); Deister et al. (1986)
$HMS + OH \xrightarrow{O_2} HCHO + SO_5^-$	$k_3 = 2.7 \times 10^8\ M^{-1}\ s^{-1}$	Olson and Fessenden (1992)
$SO_2 + O_3 \rightarrow SO_4^{2-} + O_2$	$R_{aq} = \left(k_1 x_{SO_2 \cdot H_2O} + k_2 x_{HSO_3^-} + k_3 x_{SO_3^{2-}}\right)[O_3]_{aq}[SO_2^T]_{aq}$ $k_1 = 2.4 \times 10^4\ M^{-1}\ s^{-1}$ $k_2 = 3.7 \times 10^5 \times \exp\left(-5530 \times (1/T - 1/298)\right)\ M^{-1}\ s^{-1}$ $k_3 = 1.5 \times 10^9 \times \exp\left(-5280 \times (1/T - 1/298)\right)\ M^{-1}\ s^{-1}$	Seinfeld and Pandis (2016)
$SO_2 + H_2O_2 \rightarrow SO_4^{2-} + H_2O$	$R_{aq} = k_4 K_{s1} x_{SO_2 \cdot H_2O}[H_2O_2]_{aq}[SO_2^T]_{aq}$ For cloud water, $k_4 =$ $7.45 \times 10^7 \times \exp\left(-4430 \times (1/T - 1/298)\right)/(1 + 13[H^+])\ M^{-2}\ s^{-1}$ For aerosol water, k_4 is multiplied by an enhancement factor EF that is dependent on μ_b: $EF = \begin{cases} 1.5, 0 < \mu_b \le 4 \\ 2.3\exp\left(2.4\log_{10}\mu_b - 1.2\right), \mu_b > 4 \end{cases}$	Seinfeld and Pandis (2016); Liu et al. (2020); note *a*
$SO_2 + O_2 \xrightarrow{Mn^{2+}, Fe^{3+}} SO_4^{2-}$	$R_{aq} = k_5[H^+]^{-0.74}[Mn^{2+}][Fe^{3+}][SO_2^T]_{aq}$ (pH < 4.2) $R_{aq} = k_6[H^+]^{0.67}[Mn^{2+}][Fe^{3+}][SO_2^T]_{aq}$ (pH ≥ 4.2) $k_5 = 3.7 \times 10^7 \times \exp\left(-8400 \times (1/T - 1/297)\right) \times 10^{-3\sqrt{\mu}}\ M^{-2}\ s^{-1}$ $k_6 = 2.5 \times 10^{13} \times \exp\left(-8400 \times (1/T - 1/297)\right) \times 10^{-3\sqrt{\mu}}\ M^{-2}\ s^{-1}$	Shao et al. (2019); note *b*
$SO_2 + 2NO_2 \rightarrow SO_4^{2-} + 2HONO$	$R_{aq} = k_7[NO_2]_{aq}[SO_2^T]_{aq}$ $k_7 = 1.4 \times 10^5\ M^{-1}s^{-1}$ (pH < 5) $k_7 = 8.4 \times 10^{-3}[H^+]^{-1.444}\ M^{-1}s^{-1}$ (5 ≤ pH ≤ 5.8) $k_7 = 2 \times 10^6\ M^{-1}s^{-1}$ (pH > 5.8)	Cheng et al. (2016); note *c*
$SO_2 + HONO \rightarrow SO_4^{2-} + \frac{1}{2}N_2O$	$R_{aq} = k_8[H^+]^{0.5}[HNO_2^T]_{aq}[SO_2^T]_{aq}$ $k_8 = 142\ M^{-1}s^{-1}$	Martin et al. (1981); note *d*
$SO_2 + HOBr \rightarrow SO_4^{2-} + HBr$	$R_{aq} = k_9 x_{SO_3^{2-}}[HOBr]_{aq}[SO_2^T]_{aq}$ $k_9 = 5 \times 10^9\ M^{-1}\ s^{-1}$	Troy and Margerum (1991); note *e*

The chemical reaction equations are used to indicate major reactants and products and may not be balanced in terms of stoichiometry and charge.
$x_{SO_2 \cdot H_2O} = [SO_2 \cdot H_2O]/[SO_2^T]_{aq} = [H^+]^2/([H^+]^2 + K_{s1}[H^+] + K_{s1}K_{s2})$

[a] EF is obtained by fitting the experimental data shown in Fig. 2C in Liu et al. (2020). μ_b is the molality-based ionic strength (mol kg^{-1}).

[b] The relationship between k and μ is: $k/k^{\mu=0} = 10^{b\left(\sqrt{\mu}/(1+\sqrt{\mu})\right)} \approx 10^{b\sqrt{\mu}}$, in which b is in range of −4 to −2 (Shao et al., 2019).

[c] k_7 is believed to be the lower limit (Cheng et al., 2016).

[d] $[HNO_2^T]_{aq}$ is the total dissolved HONO and NO_2^-.

[e] k_9 is determined at 25 °C, μ = 0.5 M. We consider the reaction of HOBr and SO_3^{2-} but not the one between HOBr and HSO_3^-, which is included in the standard GEOS-Chem model. The original lab experiments (Liu, 2002) seemed to be interfered by Br_2, a stronger oxidizing reagent which also reacts with HSO_3^-. A recent study by Liu and Abbatt (2020) suggested that the rate constant of HOBr and HSO_3^- was much lower that of HOBr and SO_3^{2-}.

Table 2. Equilibrium reactions.

Reaction	Constant expression	Reference and note
$SO_{2(g)} + H_2O \leftrightarrow SO_2{\cdot}H_2O$	$H = 1.3 \times \exp\left(3100 \times (1/T - 1/298)\right)$ M atm^{-1}	Sander (2015)
$SO_2{\cdot}H_2O \leftrightarrow HSO_3^- + H^+$	$K_{s1} = 1.3 \times 10^{-2} \times \exp\left(2000 \times (1/T - 1/298)\right)$ M	Seinfeld and Pandis (2016)
$HSO_3^- \leftrightarrow SO_3^{2-} + H^+$	$K_{s2} = 6.6 \times 10^{-8} \times \exp\left(1500 \times (1/T - 1/298)\right)$ M	Seinfeld and Pandis (2016)
$H_2O \leftrightarrow OH^- + H^+$	$K_w = 1.0 \times 10^{-14} \times \exp\left(-6710 \times (1/T - 1/298)\right)$ M^2	Seinfeld and Pandis (2016)
$HCHO_{(g)} \leftrightarrow HCHO_{(aq)}$	$H = 2.5 \times \exp\left(3300 \times (1/T - 1/298)\right)$ M atm^{-1}	Song et al. (2019a)
$HCHO_{(aq)} + H_2O \leftrightarrow CH_2(OH)_2$	$K_h = 1.3 \times 10^3 \times \exp\left(3800 \times (1/T - 1/298)\right)$ $k_h = 2 \times 10^5 \times \exp(-2900/T)$ s^{-1} $k_{dh} = k_h/K_h$ s^{-1}	Song et al. (2019a)
$O_{3(g)} \leftrightarrow O_{3(aq)}$	$H = 1.13 \times 10^{-2} \times \exp\left(2500 \times (1/T - 1/298)\right)$ M atm^{-1}	Sander (2015)
$H_2O_{2(g)} \leftrightarrow H_2O_{2(aq)}$	$H = 9.1 \times 10^4 \times \exp\left(6900 \times (1/T - 1/298)\right)$ M atm^{-1}	Sander (2015)
$H_2O_{2(aq)} \leftrightarrow H^+ + HO_2^-$	$K = 2.2 \times 10^{-12} \times \exp\left(-3730 \times (1/T - 1/298)\right)$ M	Seinfeld and Pandis (2016)
$NO_{2(g)} \leftrightarrow NO_{2(aq)}$	$H = 1.3 \times 10^{-2} \times \exp\left(2500 \times (1/T - 1/298)\right)$ M atm^{-1}	Sander (2015)
$HONO_{(g)} \leftrightarrow HONO_{(aq)}$	$H = 48 \times \exp\left(4800 \times (1/T - 1/298)\right)$ M atm^{-1}	Sander (2015)
$HONO_{(aq)} \leftrightarrow H^+ + NO_2^-$	$K = 5 \times 10^{-4} \times \exp\left(-1300 \times (1/T - 1/298)\right)$ M	Seinfeld and Pandis (2016)
$HOBr_{(g)} \leftrightarrow HOBr_{(aq)}$	$H = 1.3 \times 10^2$ M atm^{-1}	Sander (2015); note *a*
$OH_{(g)} \leftrightarrow OH_{(aq)}$	$H = 32 \times \exp\left(3700 \times (1/T - 1/298)\right)$ M atm^{-1}	Sander (2015)

[a]The Henry's law constant of HOBr is very uncertain, ranging from 90 to 6000 M atm^{-1}. HOBr can undergo acid dissociation and has a pK_a of 8.65 at 25 °C. We do not consider its acid dissociation because it is only partially dissociated in the interested pH range and because of the high uncertainty of its intrinsic Henry's law constant.

Table 3. Mass accommodation coefficients on aqueous surfaces.

Species	α (dimensionless)	Reference and note
SO_2	$[1 + \exp(14.7 - 3825/T)]^{-1}$	Boniface et al. (2000)
O_3	0.04	Müller and Heal (2002); note *a*
H_2O_2	0.23	Seinfeld and Pandis (2016)
HCHO	0.04	Davidovits et al. (2006)
NO_2	2×10^{-4}	Shao et al. (2019)
HONO	0.09	Davidovits et al. (2006)
HOBr	0.6	Shao et al. (2019)

[a]The α of O_3 is very uncertain with the upper limit approaches unity.

Table 4. Description of model simulations.

Abbreviation	Description
GC12.7.0	Standard GEOS-Chem version 12.7.0
GC12.1.0	Standard GEOS-Chem version 12.1.0
CTRL	Control simulation; major changes to GC12.1.0: adding cloud HMS chemistry and cloud reactions of SO_2 with HONO and NO_2 and applying some wet process updates
DFLT	Default simulation; major changes to CTRL: improving treatments of entrainment/detrainment and heterogeneous cloud sulfur chemistry and adding aerosol water reaction of SO_2 with H_2O_2; shorter time step for calculating cloud sulfur reactions
All the ten sensitivity simulations are based on DFLT with changes in individual parameters or processes	
HiKf	High k_f (HMS formation rate constant); the low k_f is used in DFLT
HiKd	High k_d (HMS decomposition rate constant); k_d is increased by a factor of 2
HiOH	High $[OH]_{aq}$ in cloud water; $[OH]_{aq}$ is increased by a factor of 10 leading to a faster HMS oxidation in clouds
CWpH	Cloud water pH; its calculations do not consider Ca^{2+}, Mg^{2+}, Na^{+}, Cl^{-}, NO_2^{-}, $HCOO^{-}$, and CH_3COO^{-}
AWOH	Aerosol water HMS oxidation by $[OH]_{aq}$; the same $[OH]_{aq}$ and oxidation rate constant are used with cloud HMS chemistry
AWK0	Aerosol water HMS formation and decomposition; the same k_f and k_d are used with cloud HMS chemistry
AWKE	Aerosol water HMS formation and decomposition; the same k_d with cloud HMS chemistry is used whereas the k_f is enhanced relative to dilute solutions by the same EF for the reaction of SO_2 and H_2O_2 in aerosol water
Three sensitivity simulations below focus on the region of East Asia	
HiNH3	High NH_3 emissions; anthropogenic NH_3 emissions in the MEIC inventory are increased by 50%
HiFA	High HCHO emissions; transportation and residential HCHO emissions in the MEIC inventory are increased by a factor of 5
AppHet	Apparent heterogeneous chemistry for SO_4^{2-} production; it is applied over East Asia (97.5°E–152.5°E, 16°N–56°N) during the cold season (November–March)

Table 5. Comparison between observations and model simulations.

Location	Year and season	Observed molar ratio	Default	Control	Reference and note
New Mexico, USA	1997 Summer	$HMS/SO_4^{2-} < 0.2\%$	0.3%	2%	Dixon and Aasen (1999); note *a*
Germany	2009/10 All Year	$HMS/SO_4^{2-} = 2\%$	5%	16%	Scheinhardt et al. (2014); note *b*
Beijing, China	2015/16 and 2016/17 Winter	$HMS/SO_4^{2-} = 11\%$	13%	10%	Ma et al. (2020); note *c*
Osaka Bay, Japan	1998/99 Spring, Summer	HMS/MSA = 1	3	20	Suzuki et al. (2001); note *d*

[a]PM_1 (particles smaller than 1 μm) samples of 11 were collected with each sampled for several days. HMS detection method: ion chromatography.
[b]Size-segregated (5 stages under 10 μm) daily aerosol samples of 154 data sets were collected at 9 sites. HMS detection method: capillary electrophoresis.
[c]$PM_{2.5}$ samples of 77 were collected with 69 daily and 8 half-day samples. HMS detection method: ion chromatography.
[d]Size-segregated (4 stages under 7 μm) aerosol samples of 4 data sets were collected with each sampled for 11–25 days. HMS detection method: proton nuclear magnetic resonance (^1H NMR).

Formatted: Superscript